

PAPER

## An experimental study on the thermal characteristics of NS-DBD plasma actuation and application for aircraft icing mitigation

To cite this article: Yang Liu *et al* 2019 *Plasma Sources Sci. Technol.* **28** 014001

View the [article online](#) for updates and enhancements.




**IOP ebooks™**

Bringing you innovative digital publishing with leading voices to create your essential collection of books in STEM research.

Start exploring the collection - download the first chapter of every title for free.

# An experimental study on the thermal characteristics of NS-DBD plasma actuation and application for aircraft icing mitigation

Yang Liu<sup>1</sup> , Cem Kolbaker<sup>1</sup>, Andrey Y Starikovskiy<sup>2</sup> , Richard Miles<sup>2</sup> and Hui Hu<sup>1,3</sup>

<sup>1</sup> Department of Aerospace Engineering, Iowa State University, 2271 Howe Hall, Room 1200, Ames, IA 50011, United States of America

<sup>2</sup> Department of Mechanical and Aerospace Engineering, Princeton University, Princeton, NJ 08544, United States of America

E-mail: [huhui@iastate.edu](mailto:huhui@iastate.edu)

Received 31 May 2018, revised 25 October 2018

Accepted for publication 2 November 2018

Published 7 January 2019



## Abstract

A comprehensive study was performed to explore the thermal characteristics of NS-dielectric-barrier discharge (DBD) plasma actuation over an airfoil/wing surface and evaluate the anti-/de-icing performance of NS-DBD plasma actuators for aircraft in-flight icing mitigation. While the fundamentals of thermal energy generation and heat transfer in NS-DBD plasma actuation over the airfoil/wing model were described in great details, a series of experiments were conducted to evaluate the effects of different environmental parameters on the heating efficiency of NS-DBD plasma actuators over the airfoil/wing surface. With the temporally-synchronized-and-spatially-resolved high-speed visualization and infrared imaging system, not only the transient thermal characteristics of NS-DBD plasma actuation over the airfoil/wing surface were revealed, but also the anti-icing performances of the NS-DBD plasma actuators were evaluated under different icing conditions, i.e. rime, mixed, and glaze. The impacts of incoming airflow velocity, air temperature, and angle of attack of the airfoil/wing model on the thermal characteristics of NS-DBD plasma actuation over the airfoil/wing surface were systematically investigated based on the measurement results. It was found that the thermal characteristics of NS-DBD plasma actuation over the airfoil/wing surface are closely coupled with the boundary layer airflow and the unsteady heat transfer process over the airfoil/wing model exposed in the frozen-cold airflows. The anti-icing performances of the NS-DBD plasma actuators under the different icing conditions were found to be varying significantly due to the variations of surface heating efficiency of the NS-DBD plasma actuators. The anti-/de-icing performance of the NS-DBD plasma actuators was found to be improved dramatically by increasing the operating frequency of the plasma actuators. The findings derived from the present study are very helpful to explore/optimize design paradigms for the development of novel plasma-based anti-/de-icing strategies tailored specifically for aircraft inflight icing mitigation to ensure safer and more efficient aircraft operation in atmospheric icing conditions.

Keywords: NS-DBD plasma actuation, thermal characteristics, heat transfer, aircraft icing

## 1. Introduction

Ice accretion on aircraft is one of the most serious hazards to flight safety in cold weathers. Aircraft flying in cold climates

would encounter icing events when the super-cooled water droplets suspended in the air impact on aircraft surfaces [1]. The rapid ice formation and accretion on aircraft surfaces would dramatically change the original profiles of aircraft wings, which can significantly decrease the lift and increase the drag of aircraft in icing conditions [2]. Though many

<sup>3</sup> The author to whom any correspondence should be addressed

efforts have been made in the past decades to investigate the ice accretion phenomena on aircraft surfaces [3–8], aircraft icing remains an important unsolved problem that is threatening the flight safety in cold climates.

Over the years, a number of anti-/de-icing systems (including both active and passive methods) have been developed for aircraft icing mitigation. While most of active anti-/de-icing methods require energy expenditure [9] or the use of deicer chemicals [10], passive anti-icing strategies are mainly dependent on the utilization of specialized hydro- and ice-phobic coatings/materials [11–16]. Although the goal of reducing/preventing ice accretion on the surfaces of airplanes has been achieved by using these techniques, they are suffering from various drawbacks. For example, the extensive use of de-icing fluids at airports has caused significant environmental pollutions to soil and underground water due to the deposition and dissipation of aqueous solutions of propylene and ethylene glycol along with other chemical additives [10]. Mechanical (e.g. pneumatic) and ultrasonic-based anti-/de-icing systems have been used to break off ice chunks accreted on aircraft surfaces, which may pose foreign object damage hazards to aero-engines [9]. The hydro- and ice-phobic coatings/materials that have been demonstrated to be icephobic in static laboratory tests are found to be unreliable (i.e. especially for the aircraft in-flight icing scenarios with high-speed impacts of super-cooled water droplets onto aircraft surfaces) and have very poor durability in repelling ice accretion due to the rapid degradation of the coatings/surfaces under harsh icing conditions [16, 17]. While electro-thermal anti-/de-icing systems have been used to melt out ice by heating aircraft surfaces [18–20], they are usually very inefficient and have demanding power requirements. Thus, it is highly desirable to develop novel anti-/de-icing techniques with less complexity, power requirement, and adverse environmental impacts for aircraft icing mitigation.

In recent years, a novel plasma-based anti-/de-icing technique has been proposed by utilizing the thermal effects induced in Dielectric-Barrier Discharge (DBD) plasma actuation [21, 22]. DBD plasma actuation is a type of discharge producing an ionized gas at the dielectric surface when high amplitude and high frequency of Alternative Current (AC) voltage, i.e. AC-DBD, or nanosecond-scale pulsed voltage, i.e. NS-DBD, is applied between two electrodes separated by a dielectric layer [23]. As a widely used flow control method, DBD plasma actuation has drawn extensive attentions in the aerospace community over the past decades [24–26]. Numerous studies have been conducted to improve the efficiency of DBD plasma actuators in flow separation control and modulation of boundary layer transition [23]. DBD plasma actuators are usually designed to be located at the leading-edge regions of airfoils/wings where the aerodynamic characteristics alter greatly as the incoming flow changes. It should be noted that, such aerodynamically delicate regions are always the preferential sites for aircraft in-flight ice accretion in cold weathers [22]. By utilizing the intense thermal effects during the plasma discharge [27, 28], DBD plasma actuators are suggested to be a promising candidate for both flow control and icing mitigation on aircraft.

It should be noted that, while DBD plasma actuation has been demonstrated to be able to reduce/prevent ice accretion on airfoil/wing surfaces efficiently [29], almost all the previous studies have focused on AC-DBD plasma actuation [21, 22]. In comparison to AC-DBD plasma actuation, NS-DBD plasma actuation has been found to have a much higher power density and faster gas heating effect during plasma discharge, which can result in a ring of expansion waves and compressive waves propagating with the velocity of sound [30]. By utilizing the ultra-fast heating mechanisms of NS-DBD plasma actuation, some preliminary studies have been performed [31, 32] to demonstrate the feasibility of utilizing NS-DBD plasma actuators for aircraft icing mitigation. However, the thermal characteristics of NS-DBD plasma actuation and their coupling effects on the unsteady heat transfer and boundary layer airflow over ice accreting airfoil/wing surfaces are never explored, which is of great importance in understanding the relevant underlying mechanisms for aircraft icing mitigation.

In the present study, an experimental investigation was conducted to examine the thermal characteristics of NS-DBD plasma actuation over an airfoil/wing surface under various experimental conditions in order to gain further insight into the underlying physics for a better understanding about the coupling effects of NS-DBD plasma actuation on the characteristics of the unsteady heat transfer and boundary layer airflow over the ice accreting airfoil/wing surfaces. The anti-/de-icing performances of the NS-DBD plasma actuators were also evaluated with the airfoil/wing model being exposed in different icing conditions (i.e. rime, mixed, and glaze). The impacts of incoming airflow velocity, air temperature, and angle of attack (AOA) of the airfoil/wing model on the thermal characteristics of NS-DBD plasma actuation as well as the anti-/de-icing performances of the NS-DBD plasma actuators at different operating frequencies were systematically investigated in order to explore/optimize design paradigms for the development of novel plasma-based anti-/de-icing strategies tailored specifically for aircraft inflight icing mitigation. In the text that follows, the fundamental basis and theories for the thermal energy generation and heat transfer in NS-DBD plasma actuation are described in great details at first. Then, the experimental setup and measurement system used in the present study will be illustrated. While the measurement results will be presented, discussions will also be given to analyze the findings derived from the present study, in comparison with those reported in previously published literatures.

## 2. Thermal energy generation in NS-DBD plasma actuation

Previous studies [30, 33, 34] have demonstrated that NS-DBD plasma actuation would induce an ultra-fast gas heating during the nanosecond high-voltage discharge, which can dramatically affect the kinetics of chemical reactions and lead to the development of shockwaves in the near-surface gas layer. When the nanosecond-pulsed high-voltage signals are

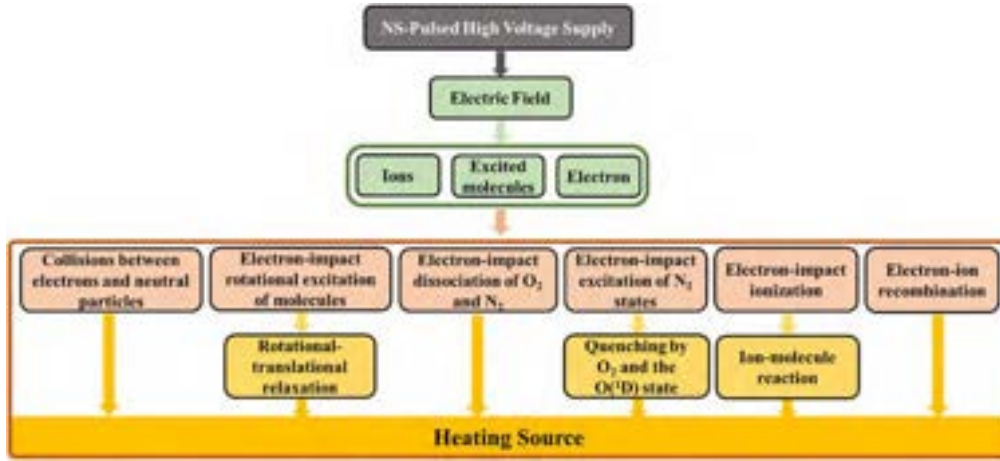
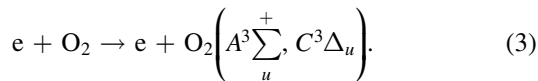
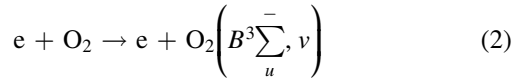


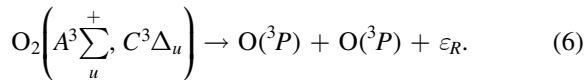
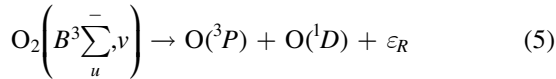
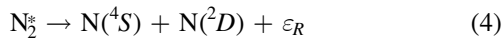
**Figure 1.** Gas heating mechanisms in NS-DBD plasma actuation.

applied to the electrodes, a high-intensity electric field would be generated between the exposed electrode and the grounded electrode separated by the dielectric layer. Driven by the electric field, the free electrons and ions in the air are responsible for energy transmission from the external power source to gas heating [30, 35]. As suggested by Popov [36] and Aleksandrov *et al* [37], the dynamics of gas heating during the plasma discharge are mainly caused by the complex collisions, reactions, and interactions between electrons, ions, and the excited molecules generated in the electrical field as illustrated in figure 1.

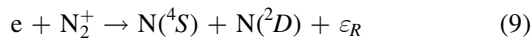
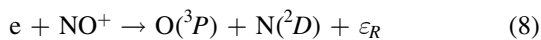
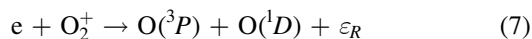
When the free electrons impact the molecules in the air (e.g.  $N_2$  and  $O_2$ ), these molecules would be excited from the ground states to the electronic states:



Then, dissociation of the excited molecules would occur, generating a significant amount of thermal energy [36]:

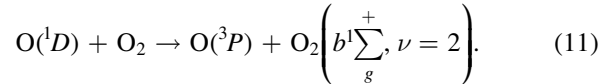
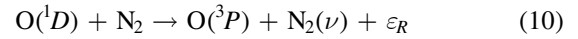


When electrons impact with the molecular ions in the electrical field, recombination would also occur [37]:

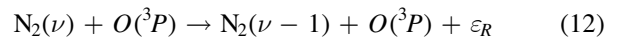


during which processes, the energy would be released between the electronic and translational degrees of freedom of the produced atoms [36].

During the dissociation processes of the electronically excited molecules, while the energy released in the collisions is expended on the rotational excitation of molecules and gas heating, the rotational energy is relaxed into the translational degrees of freedom during the multiple collisions, which is termed as quenching of the excited molecules. The kinetic energy produced in the quenching processes is rapidly converted into gas heating [36]. More details on the quenching reactions of the electronically excited molecules can be found in Popov [36]. It should be noted that a large number of excited oxygen atoms  $O(^1D)$  are produced in the dissociation/recombination/quenching reactions. These excited atoms can also be quenched by the molecules in the air, i.e.  $N_2$  and  $O_2$ :



It is suggested about 70% of the excitation energy of the excited atoms  $O(^1D)$  is expended on gas heating [36]. Along with the above dissociation and quenching reactions, the excited oxygen atoms  $O(^3P)$  would also lead to the reaction of VT relaxation:



which is considered to be a significant reaction contributing to the gas heating.

### 3. Heat transfer in NS-DBD plasma actuation

#### 3.1. Heat transfer processes over the airfoil/wing surface during nS-DBD plasma actuation

While many previous studies have revealed the mechanisms of ultra-fast gas heating in NS-DBD plasma actuation [36–38], they were mostly derived in the condition of plasma actuation over a flat plate in still air, very few was conducted to investigate the very complex heat transfer process in NS-DBD plasma actuation over an airfoil/wing surface exposed in different airflow velocity and air temperature conditions,

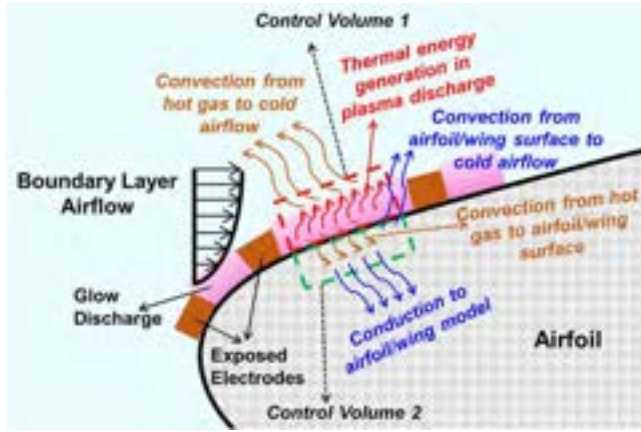


**Figure 2.** A schematic of the thermal energy generation and heat transfer process over an airfoil/wing surface embedded with NS-DBD plasma discharge.

especially in frozen-cold airflow conditions that are conducive to icing events. In the present study, a theoretic model of heat transfer is developed, as the first of its kind, to reveal the contributing factors that affect the gas/surface heating processes over an airfoil/wing surface.

Figure 2 shows a schematic of the thermal energy generation and heat transfer process over an airfoil/wing surface embedded with NS-DBD plasma discharge. Two adjacent control volumes are selected at the discharge region (Control Volume 1, i.e. CV1) and the airfoil/wing surface (Control Volume 2, i.e. CV2) as illustrated in figure 2. Based on the classic energy conservation law [39], the control volume may have thermal energy and mechanical energy instantly entering and leaving through the control volume, i.e.  $\dot{E}_{in}$  and  $\dot{E}_{out}$ . Meanwhile, thermal energy may be generated within the control volume, i.e.  $\dot{E}_g$ . Thus, the rate of energy change stored within the control volume,  $\dot{E}_{st}$ , can be expressed in a general form as given in equation (13).

$$\dot{E}_{st} = \frac{dE_{st}}{dt} = \dot{E}_{in} + \dot{E}_g - \dot{E}_{out}. \quad (13)$$

The energy change stored within the control volume are essentially due to the changes in the internal, kinetic, and/or potential energies of its contents:

$$\Delta E_{st} = \Delta U + \Delta KE + \Delta PE, \quad (14)$$

where  $\Delta U$ ,  $\Delta KE$ , and  $\Delta PE$  are representing the changes in the internal energy, kinetic energy, and potential energy.

For the case of plasma discharge over the airfoil/wing surface, the changes of kinetic and potential energies inside the two control volumes are very small and can be neglected. Thus, the energy changes stored in the two control volumes are mainly

the internal energies,  $\Delta U_1$  and  $\Delta U_2$  ( $U_1 = \rho_{gas} V_1 c_{gas} T_{gas}$ , where  $\rho_{gas}$  and  $c_{gas}$  are the mass density and the specific heat of the gas in CV1;  $U_2 = \rho_{surf} V_2 c_{surf} T_{surf}$ , where  $\rho_{surf}$  and  $c_{surf}$  are the mass density and the specific heat of the surface material in CV2). The energy change in CV1 is mainly the disparity between the thermal energy generation in plasma discharge and the heat dissipation (i.e. heat transfer from the hot gas in CV1 to the cold airflow and the airfoil/wing surface). The rate of energy change stored in CV1, therefore, can be expressed as:

$$\frac{dU_1}{dt} = \dot{Q}_{dis} - [\dot{Q}_{gas \rightarrow air} + \dot{Q}_{gas \rightarrow surf}], \quad (15)$$

where  $\dot{Q}_{dis}$  is the rate of thermal energy generation in plasma discharge,  $\dot{Q}_{gas \rightarrow air}$  and  $\dot{Q}_{gas \rightarrow surf}$  are the rates of convective heat transfer to the cold airflow and the airfoil/wing surface, respectively.

The rate of convective heat transfer from the hot gas in CV1 to the cold airflow can be expressed as:

$$\dot{Q}_{gas \rightarrow air} = h_{cv-air} \cdot (T_{gas} - T_{air,\infty}) \cdot A, \quad (16)$$

where  $h_{cv-air}$  is the convective heat transfer coefficient between the hot gas and the cold airflow,  $T_{gas}$  is the temperature of the hot gas in CV1,  $T_{air,\infty}$  is the airflow temperature, and  $A$  is the projected surface area of CV1. The rate of convective heat transfer from the hot gas to the airfoil/wing surface can be expressed in a similar form:

$$\dot{Q}_{gas \rightarrow surf} = h_{cv-surf} \cdot (T_{gas} - T_{surf}) \cdot A, \quad (17)$$

where  $h_{cv-surf}$  is the convective heat transfer coefficient between the hot gas and airfoil/wing surface,  $T_{surf}$  is the temperature of the airfoil/wing surface.

Thus, equation (15) can be expanded in the form of equation (18)

$$\begin{aligned} \frac{dU_1}{dt} = \rho_{gas} V_1 c_{gas} \frac{dT_{gas}}{dt} = \dot{Q}_{dis} - A [T_{gas} (h_{cv-air} + h_{cv-surf}) \\ - (h_{cv-air} T_{air,\infty} + h_{cv-surf} T_{surf})]. \end{aligned} \quad (18)$$

Hence,

$$\frac{dT_{gas}}{dt} = \frac{\dot{Q}_{dis} - A [T_{gas} (h_{cv-air} + h_{cv-surf}) - (h_{cv-air} T_{air,\infty} + h_{cv-surf} T_{surf})]}{\rho_{gas} V_1 c_{gas}}. \quad (19)$$

The energy change in CV2 is essentially a result of the energy input from the hot gas in CV1 to the airfoil/wing surface and the energy loss due to the heat transfer from the airfoil/wing surface to the cold airflow and the heat dissipation in the airfoil/wing model.

$$\frac{dU_2}{dt} = \dot{Q}_{gas \rightarrow surf} - [\dot{Q}_{surf \rightarrow air} + \dot{Q}_{cond}], \quad (20)$$

where  $\dot{Q}_{surf \rightarrow air}$  is the rate of convective heat transfer from the airfoil/wing surface to the cold airflow;  $\dot{Q}_{cond}$  is the rate of heat dissipation in the airfoil/wing model.



The rate of convective heat transfer from the airfoil/wing surface to the cold airflow can be expressed as:

$$\dot{Q}_{\text{surf} \rightarrow \text{air}} = h_{\text{cv-surf}} \cdot (T_{\text{surf}} - T_{\text{air},\infty}) \cdot A. \quad (21)$$

The rate heat dissipation into the airfoil/wing model is:

$$\dot{Q}_{\text{cond}} = \frac{A \cdot (T_{\text{surf}} - T_{\text{airfoil}})}{k_{\text{airfoil}}}. \quad (22)$$

Therefore, the rate of energy change stored in CV2 can be expressed as:

$$\begin{aligned} \frac{dU_2}{dt} &= \rho_{\text{surf}} V_2 c_{\text{surf}} \frac{dT_{\text{surf}}}{dt} \\ &= A \left[ h_{\text{cv-surf}} (T_{\text{gas}} - 2T_{\text{surf}} + T_{\text{air},\infty}) - \frac{(T_{\text{surf}} - T_{\text{air},\infty})}{k_{\text{airfoil}}} \right]. \end{aligned} \quad (23)$$

Hence,

$$\begin{aligned} \frac{dT_{\text{surf}}}{dt} &= \frac{A}{\rho_{\text{surf}} V_2 c_{\text{surf}}} \left[ h_{\text{cv-surf}} (T_{\text{gas}} - 2T_{\text{surf}} + T_{\text{air},\infty}) \right. \\ &\quad \left. - \frac{(T_{\text{surf}} - T_{\text{air},\infty})}{k_{\text{airfoil}}} \right]. \end{aligned} \quad (24)$$

Based on the derived temperature change rate of the hot gas layer and the airfoil/wing surface as given in equations (19) and (24), it is found that while the hot gas temperature in the plasma region and the airfoil/wing surface temperature are interfering with each other, both of them are essentially determined by the rate of thermal energy generation in plasma discharge and the local convective heat transfer coefficients of the hot gas layer and the airfoil/wing surface (which are greatly influenced by the airflow velocity, temperature, and the AOA of the airfoil/wing model). It should be noted that, when the control volumes (i.e. CV1 and CV2) reach the thermal equilibrium state, the temperatures of the hot gas layer and the airfoil/wing surface would become constant. Thus, the temperature change rate given in equations (19) and (24) would become zero:

$$\frac{dT_{\text{gas}}}{dt} = \frac{\dot{Q}_{\text{dis}} - A[T_{\text{gas}}(h_{\text{cv-air}} + h_{\text{cv-surf}}) - (h_{\text{cv-air}}T_{\text{air},\infty} + h_{\text{cv-surf}}T_{\text{surf}})]}{\rho_{\text{gas}} V_1 c_{\text{gas}}} = 0 \quad (25)$$

Equations (25) and (26) can be further reduced to:

$$\dot{Q}_{\text{dis}} - A[T_{\text{gas}}(h_{\text{cv-air}} + h_{\text{cv-surf}}) - (h_{\text{cv-air}}T_{\text{air},\infty} + h_{\text{cv-surf}}T_{\text{surf}})] = 0 \quad (27)$$

$$h_{\text{cv-surf}}(T_{\text{gas}} - 2T_{\text{surf}} + T_{\text{air},\infty}) - \frac{(T_{\text{surf}} - T_{\text{air},\infty})}{k_{\text{airfoil}}} = 0. \quad (28)$$

Thus, two different expressions of the hot gas temperature within CV1 at the thermal equilibrium state can be derived as shown in equations (29) and (30):

$$T_{\text{gas}} = \frac{\dot{Q}_{\text{dis}} + A(h_{\text{cv-air}}T_{\text{air},\infty} + h_{\text{cv-surf}}T_{\text{surf}})}{A(h_{\text{cv-air}} + h_{\text{cv-surf}})} \quad (29)$$

$$T_{\text{gas}} = \frac{(T_{\text{surf}} - T_{\text{air},\infty})}{k_{\text{airfoil}}h_{\text{cv-surf}}} + 2T_{\text{surf}} - T_{\text{air},\infty} \quad (30)$$

By substituting  $T_{\text{gas}}$  with equation (29) into equation (30):

$$\begin{aligned} \frac{\dot{Q}_{\text{dis}} + A(h_{\text{cv-air}}T_{\text{air},\infty} + h_{\text{cv-surf}}T_{\text{surf}})}{A(h_{\text{cv-air}} + h_{\text{cv-surf}})} &= \frac{(T_{\text{surf}} - T_{\text{air},\infty})}{k_{\text{airfoil}}h_{\text{cv-surf}}} \\ &\quad + 2T_{\text{surf}} - T_{\text{air},\infty}. \end{aligned} \quad (31)$$

Thus, the airfoil/wing surface temperature can be derived as given in equation (32)

$$\begin{aligned} T_{\text{surf}} &= T_{\text{air},\infty} \\ &\quad + \frac{k_{\text{airfoil}}\dot{Q}_{\text{dis}}}{A(h_{\text{cv-air}}/h_{\text{cv-surf}} + 1 + 2k_{\text{airfoil}}h_{\text{cv-air}} + k_{\text{airfoil}}h_{\text{cv-surf}})}. \end{aligned} \quad (32)$$

Since the initial temperature of the airfoil/wing surface is the same with the freestream airflow temperature, the surface temperature increase from the initial state to the thermal equilibrium state can be derived as given in equation (33).

$$\Delta T = \frac{k_{\text{airfoil}}\dot{Q}_{\text{dis}}}{A(h_{\text{cv-air}}/h_{\text{cv-surf}} + 1 + 2k_{\text{airfoil}}h_{\text{cv-air}} + k_{\text{airfoil}}h_{\text{cv-surf}})}. \quad (33)$$

It is clearly seen that the surface temperature increase during the plasma actuation is essentially determined by the rate of thermal energy generation in plasma discharge and the convective/conductive heat transfer coefficients under specific test conditions.

$$\begin{aligned} \frac{dT_{\text{surf}}}{dt} &= \frac{A}{\rho_{\text{surf}} V_2 c_{\text{surf}}} \left[ h_{\text{cv-surf}}(T_{\text{gas}} - 2T_{\text{surf}} + T_{\text{air},\infty}) \right. \\ &\quad \left. - \frac{(T_{\text{surf}} - T_{\text{air},\infty})}{k_{\text{airfoil}}} \right] = 0. \end{aligned} \quad (26)$$

### 3.2. Heating efficiency in NS-DBD plasma actuation

The above analysis of the unsteady heat transfer processes during the NS-DBD plasma actuation over the airfoil/wing model has highlighted the significance of thermal efficiency in plasma discharge in heating up the near-wall gas layer and

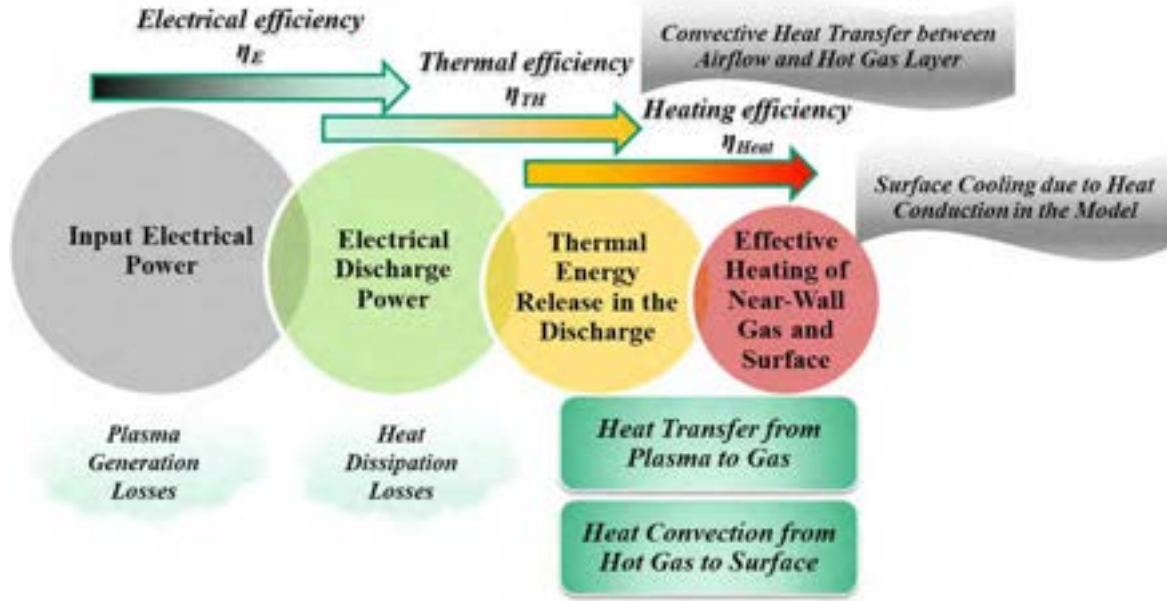


**Figure 3.** Sketch of the framework of energy conversion for NS-DBD plasma actuation in gas/surface heating.

the airfoil/wing surface. In order to further link the energy input for NS-DBD plasma actuation and the effective utilization of thermal energy for heating operations, more efforts are made in this study to build a framework of characterizing the heating efficiency in NS-DBD plasma actuation, tailored specially for aircraft icing mitigation.

As suggested by Correale *et al* [40], a NS-DBD plasma actuator usually has three stages of energy conversion in the term of flow control mechanism, i.e. (I) electrical power to discharge power,  $P_A$ ; (II) discharge power to fluid mechanic power,  $P_{FM}$ , and (III) fluid mechanic power to feedback power in flow control,  $P_C$ . Each of the three stages would have a contribution to the overall control efficiency and, meanwhile, suffer from energy losses. Thus, three efficiencies for the different stages are defined as electrical efficiency,  $\eta_E$ , fluid mechanic efficiency,  $\eta_{FM}$ , and power saving rate,  $\eta'_S$  [40]. For a given electrical input power  $P_{input}$ , the efficiencies of the first two operational stages are:

$$\eta_E = \frac{P_A}{P_{input}} \quad (34)$$

$$\eta_{FM} = \frac{P_{FM}}{P_A}. \quad (35)$$

To quantify the energy utilization of NS-DBD plasma actuation in the term of gas/surface heating, a similar approach of describing the energy conversion from input electrical power to the final effective heating of the near-wall gas and surface is formulated and sketched in figure 3. It is clearly seen that there are also three stages of operation for a NS-DBD plasma actuator to generate effective heating power: (I) electrical power to discharge power,  $P_A$ ; (II) discharge power to thermal power,  $P_{TH}$ , and (III) thermal power to effective surface heating in desired locations,  $P_{Heat}$ . While the first stage efficiency, i.e. electrical efficiency,  $\eta_E$ , is the same

with that defined in Correale *et al* [40], the second stage efficiency, i.e. thermal efficiency,  $\eta_{TH}$ , is defined as the ratio of thermal power and the discharge power:

$$\eta_{TH} = \frac{P_{TH}}{P_A}. \quad (36)$$

The third stage efficiency,  $\eta_{Heat}$ , is defined as the ratio of the effective surface heating power at the desired locations and the total thermal power:

$$\eta_{Heat} = \frac{P_{Heat}}{P_{TH}}. \quad (37)$$

During the plasma discharge, while the rate of thermal energy generation,  $\dot{Q}_{dis}$ , is almost not changed, the effective surface heating energy in CV2 can be calculated using equation (38):

$$E_{Heat} = \rho_{surf} V_2 c_{surf} \Delta T. \quad (38)$$

By substituting  $\Delta T$  with equation (33) into equation (38), the third stage efficiency of the plasma actuation in surface heating over the airfoil/wing model is derived as given in equation (39):

$$\begin{aligned} \eta_{Heat} &= \frac{\rho_{surf} V_2 c_{surf} \Delta T}{\dot{Q}_{dis} t_{heating}} \\ &= \frac{\rho_{surf} H_{surf} c_{surf} k_{airfoil}}{t_{heating} (h_{cv-air}/h_{cv-surf} + 1 + 2k_{airfoil} h_{cv-air} + k_{airfoil} h_{cv-surf})}, \end{aligned} \quad (39)$$

where  $t_{heating}$  is time duration of the surface heating process, i.e. from the initial state to the thermal equilibrium state;  $H_{surf}$  is thickness of the surface material (i.e. dielectric layer).

It is suggested that the surface heating efficiency in plasma discharge is essentially determined by the surface material properties (i.e. the density, thickness, and heat capacity of the dielectric layer) and the conductive/convective heat transfer

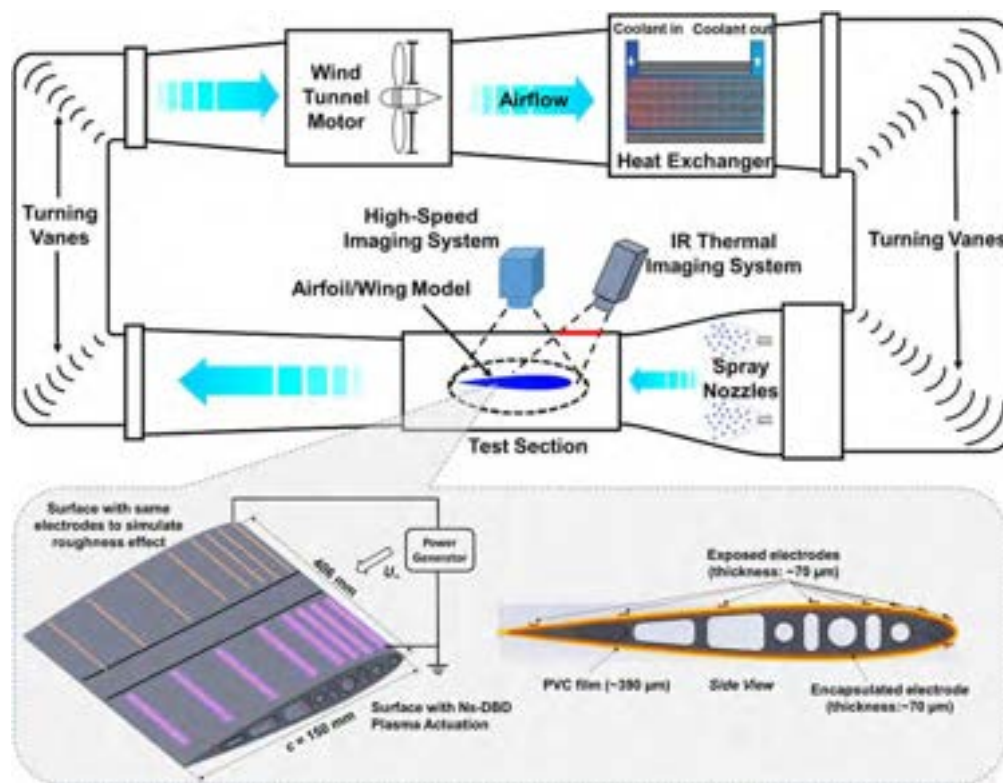


**Figure 4.** Schematic of the ISU-IRT and the airfoil/wing model used for the impact icing experiment.

coefficients, but in regardless of the rate of thermal energy generation.

#### 4. Experimental setup and test model

The experimental study to characterize the thermal effects in NS-DBD plasma actuation was performed in the unique Icing Research Tunnel available at Aerospace Engineering Department of Iowa State University (i.e. ISU-IRT). As shown schematically in figure 4, ISU-IRT is a multifunctional icing research tunnel with a test section of 2.0 m in length  $\times$  0.4 m in width  $\times$  0.4 m in height with four side walls being optically transparent. It has a capacity of generating a maximum wind speed of  $60 \text{ m s}^{-1}$  and an airflow temperature down to  $-25^\circ\text{C}$ . An array of 8 pneumatic atomizer/spray nozzles are installed at the entrance of the contraction section of the icing tunnel to inject micro-sized water droplets ( $10\text{--}100 \text{ }\mu\text{m}$  in size with the MVD  $\approx 20 \text{ }\mu\text{m}$ ) into the airflow. By manipulating the water flow rate through the spray nozzles, the liquid water content (LWC) in ISU-IRT could be adjusted (i.e. LWC ranging from  $0.1$  to  $5.0 \text{ g m}^{-3}$ ). In summary, ISU-IRT can be used to simulate atmospheric icing phenomena over a range of icing conditions (i.e. from dry rime to extremely wet glaze ice conditions) [41, 42].

A NACA0012 airfoil/wing model was used in the present study, which is made of a hard-plastic material and manufactured by using a rapid prototyping machine (i.e. 3D printing) that builds 3D models layer-by-layer with a resolution of about  $25 \text{ }\mu\text{m}$ . The airfoil/wing model has a chord

**Table 1.** Emissivity of the materials pertinent to the test model used in the present study.

Materials	Emissivity
Surface of the airfoil/wing model (covered with PVC film)	0.91–0.93
Ice	0.965
Water	0.950–0.963

length of  $c = 150 \text{ mm}$ , which spanned the width of the test section of ISU-IRT. Supported by a stainless-steel rod, the airfoil/wing model was mounted at its quarter-chord and oriented horizontally across the middle of the test section.

During the experiments, the dynamic ice accreting process over the airfoil surface was recorded by using a high-speed camera (PCO Tech, Dimax) with a 60 mm lens (Nikon, 60 mm Nikkor  $f/2.8$ ) installed at 500 mm above the airfoil/wing model. The camera was positioned approximately normal to the airfoil chord, with a measurement window size of  $210 \text{ mm} \times 210 \text{ mm}$  and a spatial resolution of  $9.5 \text{ pixels mm}^{-1}$ . An *in situ* calibration procedure as suggested by Soloff *et al* [43] was performed to dewarp the captured images before extracting physical features. Each test trial consisted of 3000 images acquired at a frame rate of 10 Hz. As shown schematically in figure 2, an infrared (IR) thermal imaging camera (FLIR A615) was also used to map the surface temperature of the ice accreting airfoil surface. The IR camera was mounted at  $\sim 300 \text{ mm}$  above the airfoil/wing model with the measurement window size of  $110 \text{ mm} \times 90 \text{ mm}$  and a corresponding spatial



resolution of  $5.3 \text{ pixels mm}^{-1}$ . IR radiation from the ice accreting airfoil surface would pass through an IR window (i.e. FLIR IR Window-IRW-4C with optic material of Calcium Fluoride) and be collected by the IR thermal imaging camera. A calibration of the material emissivity is performed for the IR thermal imaging [24]. Table 1 gives the IR emissivity of the materials relevant to the present study, i.e. surface of the airfoil/wing model, ice, and liquid water, respectively. Each test trial consisted of 15 000 IR images acquired at a frame rate of 50 Hz. An *in situ* calibration was also performed to validate the IR thermal imaging results by establishing a relationship between the measured count number from the IR camera and the temperature acquired by using thermocouples. The measurement uncertainty for the IR camera was found to be about  $\pm 0.2^\circ\text{C}$ . The high-speed video camera and the IR camera were connected to a digital delay generator (Berkeley Nucleonics, model 575) that synchronized the timing between the two imaging systems.

As clearly shown in figure 4, a half-half configuration of the DBD plasma actuators (i.e. plasma on versus plasma off) was designed over the airfoil/wing model. Each of the plasma actuators consisted of one encapsulated electrode sheet and nine exposed electrodes, with the same thickness of about  $70 \mu\text{m}$  and length of  $\sim 125 \text{ mm}$ . In the present study, five layers of PVC film (i.e.  $\sim 100 \mu\text{m}$  for each layer) were integrated to serve as the dielectric barrier to separate the encapsulated electrode sheet from the exposed electrodes.

The plasma actuators were operated via an arbitrary function generator (AFG) and powered by an FID solid-state power supply capable of delivering a pulsed high voltage signal of about 23 ns, with a rising time of 3 ns (from 10% to 90% of the maximum voltage). The maximum voltage and the maximum frequency are 10 kV and 10 kHz, respectively (same power generator was used in [40]). The investigated energy input consists of a burst of 50 pulses discharged at maximum voltage and frequency. Power measurements were performed via the back-current shunt technique [40] in order to calculate energy associated with a single pulse. This is an indirect technique relying on the measure of incident and reflected current running through the actuator circuit. A shunt monitor resistor is built using 16 resistors, of  $3.2 \Omega$  each, placed in parallel, resulting in an overall shunt resistance of  $0.2 \Omega$ . The shunt resistor was placed in the middle of the ground electrode of a 20 m long high voltage coaxial cable (type RG-217). This high voltage cable is used to deliver the high voltage nanosecond pulse from the power generator to the tested plasma actuator. The shunt resistor was calibrated by applying a known signal of 5 V from an AFG (Tektronics AFG3252) and measuring the voltage across the shunt directly using a digital oscilloscope with a sampling frequency of 1 GHz set at an impedance so as to match the impedance of the high voltage cable, i.e.  $50 \Omega$ . For the actual measurements, a 20 dB signal attenuator was used to protect the oscilloscope from voltage overload. Measurements of pulse energy were performed by quantifying the voltage across the shunt resistor directly with the oscilloscope. The application of a high voltage nanosecond pulse from the power generator can be observed as a scaled voltage pulse

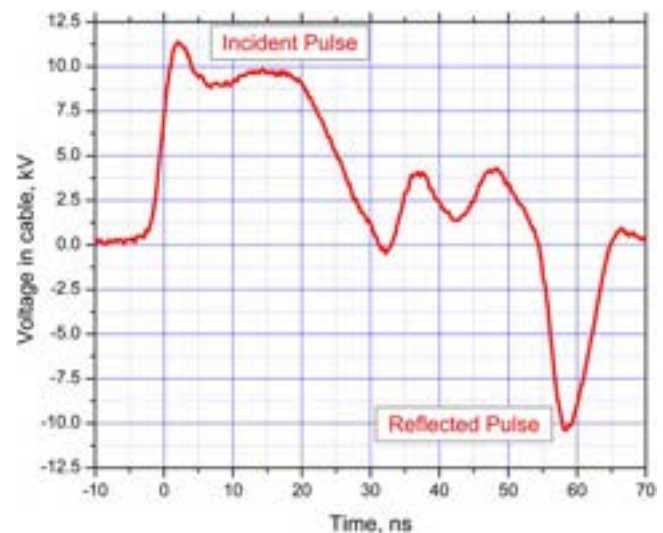


**Figure 5.** A typical high voltage driving signal calculated through the back current shunt measurements as a function of time ( $t$ ) in nanoseconds.

over the shunt, measured by the oscilloscope. A typical discharged pulse ( $V_{\text{app}}$ ) as measured across the shunt is shown in figure 5. The energy per single pulse in the discharge was calculated to be  $E = 34.5 \pm 0.1 \text{ mJ/pulse}$ . Thus, the power of the NS-DBD plasma actuators was  $P = 34.5 \text{ W}$  at  $f = 1 \text{ kHz}$ ,  $P = 69 \text{ W}$  at  $f = 2 \text{ kHz}$ ,  $P = 138 \text{ W}$  at  $f = 4 \text{ kHz}$ , and  $P = 207 \text{ W}$  at  $f = 6 \text{ kHz}$ , respectively.

In the present study, both dry (without turning on the water spray system of ISU-IRT) and icing experiments were conducted to quantify the transient thermal characteristics of NS-DBD plasma actuation in various environmental and flight conditions. Table 2 summarizes the cases tested in the present study. For NS-DBD plasma actuation, while the amount of thermal energy generation is linearly related to the pulse repetition frequency (PRF) of the actuator, a higher PRF would induce much stronger electromagnetic interference (EMI) during plasma discharge. Therefore, to avoid overheating of the airfoil/wing model and the potential damages to the electrical devices caused by EMI, a relatively low PRF (i.e.  $f = 1 \text{ kHz}$ ) of the NS-DBD plasma actuation was selected in the dry experiments. By adjusting the incoming airflow velocity, airflow temperature, and AOA of the airfoil/wing model, the impacts of the various environmental and operational parameters on the thermal characteristics of NS-DBD plasma actuation were quantitatively evaluated. For the icing experiments, while the incoming airflow velocity and the LWC level were kept as the same throughout the experiments, i.e.  $U_\infty = 40 \text{ m s}^{-1}$  and  $\text{LWC} = 1.0 \text{ g m}^{-3}$ , the airflow temperature was varied from  $-15^\circ\text{C}$  to  $-5^\circ\text{C}$  to produce three typical icing conditions (i.e. rime, mixed, and glaze icing conditions [42]) in evaluating the anti-icing performance of NS-DBD plasma actuation. In the present study, the operating frequency of the NS-DBD plasma actuators was also adjusted during the icing experiments (i.e.  $f = 2 \text{ kHz}$ ,  $4 \text{ kHz}$ , and  $6 \text{ kHz}$ ) to provide evidences of the effects of ns-pulse frequency on the anti-/de-icing performance of the plasma actuators for aircraft icing mitigation.

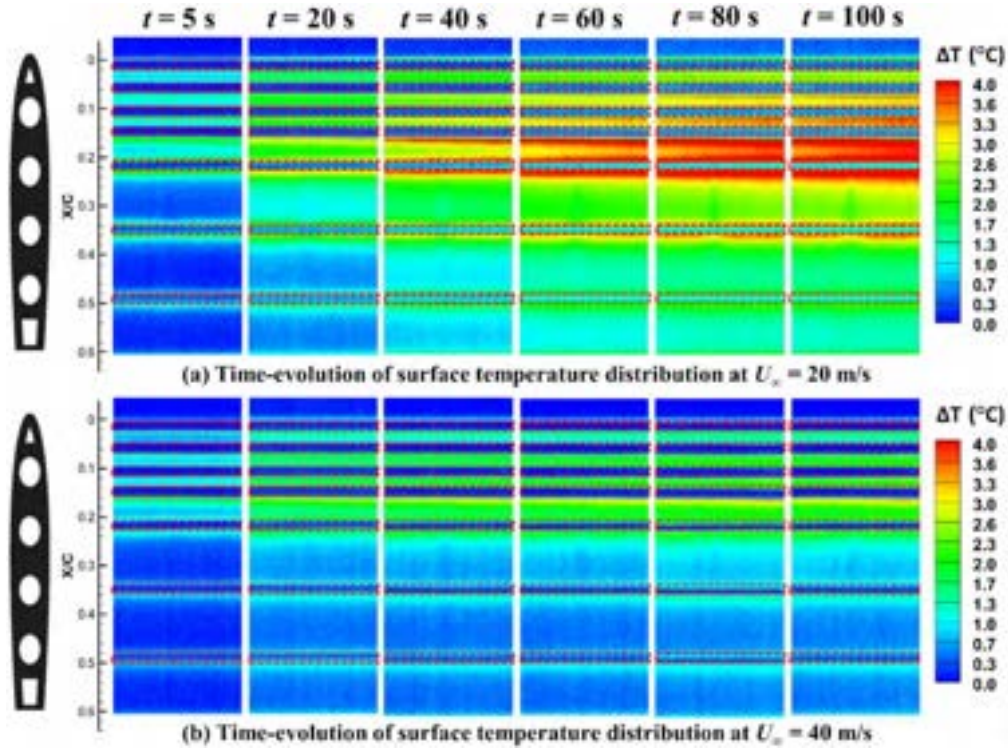


**Figure 6.** Time-evolutions of the measured surface temperature distributions over the airfoil/wing model under the test conditions of  $T_\infty = -10^{\circ}\text{C}$  and  $\text{AOA} = 0^{\circ}$ , and different incoming airflow velocities.

**Table 2.** A list of the test cases of the present study.

Case no.	State	AoA ( $^{\circ}$ )	$U_\infty$ ( $\text{m s}^{-1}$ )	$T_\infty$ ( $^{\circ}\text{C}$ )	LWC ( $\text{g m}^{-3}$ )	PRF (kHz)
1	Dry	0	20	$-10.0$	0	1
2	Dry	0	40	$-10.0$	0	1
3	Dry	0	40	$-15.0$	0	1
4	Dry	0	40	$-5.0$	0	1
5	Dry	$-5$	40	$-10.0$	0	1
6	Dry	5	40	$-10.0$	0	1
7	Icing	0	40	$-10.0$	1.0	2
8	Icing	0	40	$-10.0$	1.0	4
9	Icing	0	40	$-10.0$	1.0	6
10	Icing	0	40	$-15.0$	1.0	4
11	Icing	0	40	$-5.0$	1.0	4

**Table 3.** Properties of the PVC dielectric surface and the input power parameters.

$\rho_{\text{surf}}$ ( $\text{kg m}^{-3}$ )	$H_{\text{surf}}$ (mm)	$c_{\text{surf}}$ ( $\text{J kg}^{-1} ^{\circ}\text{C}^{-1}$ )	$A_{\text{surf}}$ ( $\text{m}^2$ )	$P_A$ (W)	$\eta_{\text{TH}}$ (-)
$1.38 \times 10^3$	0.5	1170	0.021	34.5	40%–90%

## 5. Measurement results and discussion

As mentioned above, a large amount of thermal energy would be promptly generated in NS-DBD plasma actuation, which can produce a ring of expansion and compressive waves propagating with the velocity of sound [30]. For the use of NS-DBD plasma actuation in anti-/de-icing applications, the plasma actuators are usually fabricated over airfoil/wing surfaces [32], and exposed in frozen-cold airflows that are conducive to icing

events. Thus, complex interactions between the thermal energy generation in plasma discharge, the boundary layer airflow, and the unsteady heat transfer processes would occur, which are closely coupled with the working parameters such as incoming airflow velocity, air temperature, and AOA of the airfoil/wing model. In the present study, in order to quantitatively reveal the effects of the different environmental and operational parameters (i.e. airflow velocity, temperature, and AOA of the airfoil/wing model) on the thermal characteristics of NS-DBD

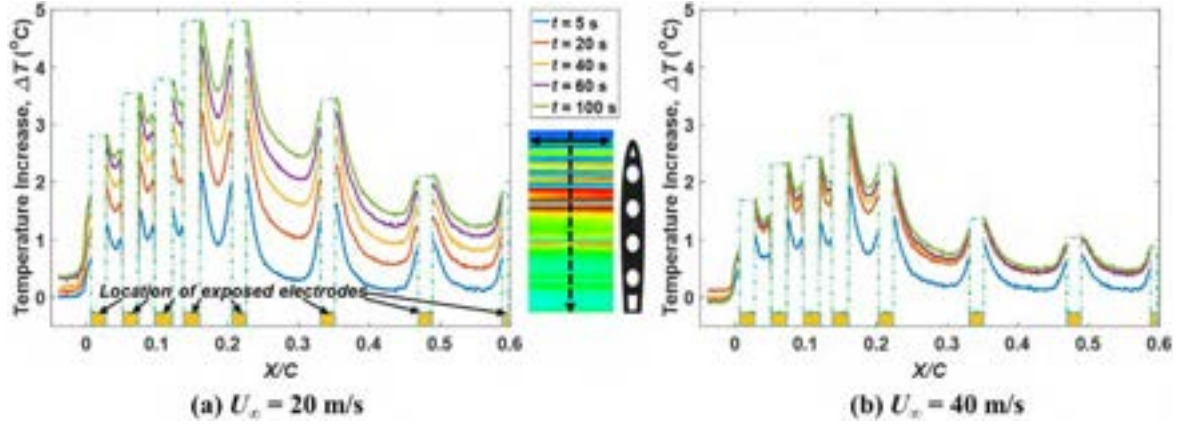


**Figure 7.** The spanwise-averaged temperature profiles along the airfoil/wing chord under the test conditions of  $T_\infty = -10^\circ\text{C}$  and  $\text{AOA} = 0^\circ$ , and different incoming airflow velocities.

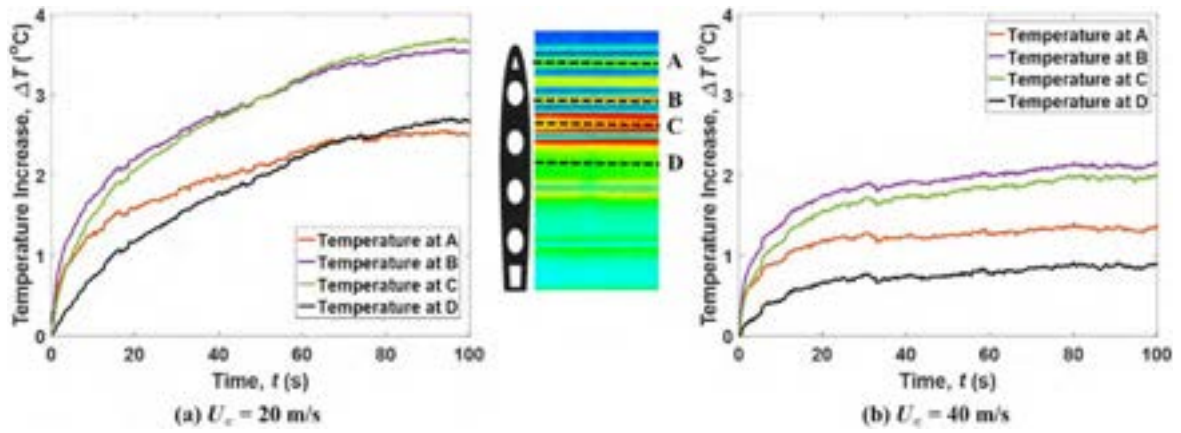


**Figure 8.** Time-evolution of the surface temperature at different chordwise locations on the airfoil/wing model under the test conditions of  $T_\infty = -10^\circ\text{C}$ ,  $\text{AOA} = 0^\circ$ , and (a)  $U_\infty = 20 \text{ m s}^{-1}$ , (b)  $U_\infty = 40 \text{ m s}^{-1}$ .

plasma actuation over the airfoil/wing surface, a series of experiments were conducted with the airflow velocity being varied from  $U_\infty = 20$  to  $40 \text{ m s}^{-1}$ , air temperature from  $T_\infty = -15^\circ\text{C}$  to  $-5^\circ\text{C}$ , and the AOA of the airfoil/wing model from  $\text{AOA} = -5^\circ$  to  $5^\circ$ .

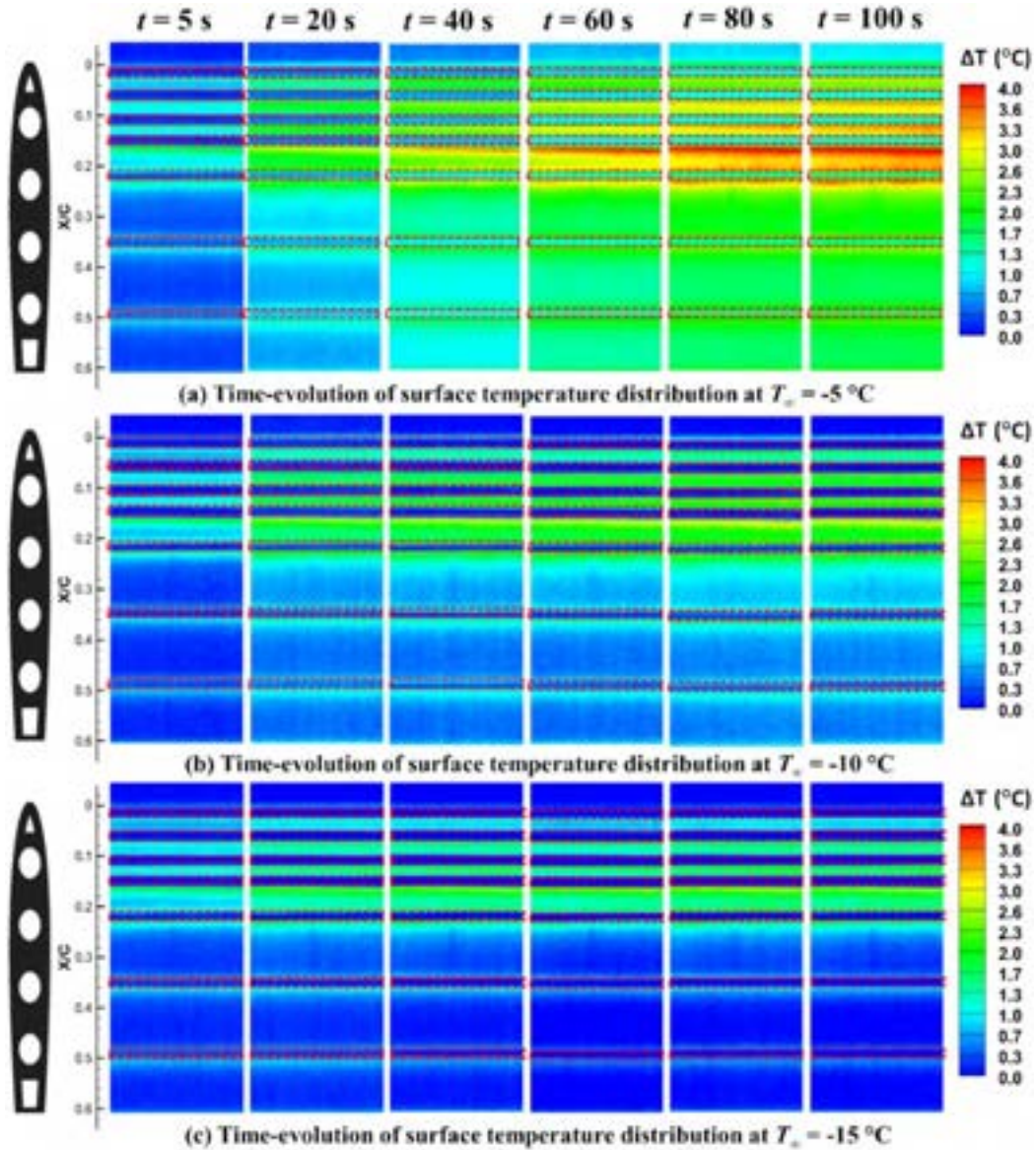
### 5.1. Effects of airflow velocity on the heating dynamics in NS-DBD plasma actuation

Figure 6 shows the time-evolutions of the measured surface temperature distributions over the airfoil/wing model with the air temperature and the AOA of the airfoil/wing model being constant at  $T_\infty = -10^\circ\text{C}$  and  $\text{AOA} = 0^\circ$ , respectively, while the incoming airflow velocity was changed from  $U_\infty = 20$  to  $40 \text{ m s}^{-1}$ . The locations of the exposed electrodes are also indicated by the red dashed boxes as given in figure 6. It is clearly seen that, as the time goes by, while the temperature distribution over the airfoil/wing surface shows a more significant increase at the lower airflow velocity, i.e.  $U_\infty = 20 \text{ m s}^{-1}$ , a thermal equilibrium state is found to be achieved earlier when the airflow velocity is higher, i.e. while the surface temperature distribution at  $U_\infty = 40 \text{ m s}^{-1}$  is found to become stable after about  $t = 40 \text{ s}$ , the temperature

distribution at  $U_\infty = 20 \text{ m s}^{-1}$  is found to be still increasing after  $t = 100 \text{ s}$ . It should also be noted that while an overall increase of the surface temperature is observed, the temperature increases near the exposed electrodes are found to be much more evident as shown in figure 6, which is consistent with the observation by Jousset *et al* [44].

Based on the measured surface temperature distributions over the airfoil/wing model as shown in figure 6, the spanwise-averaged temperature profiles along the airfoil chord at the different time instants (i.e.  $t = 5, 20, 40, 60$ , and  $100 \text{ s}$ ) are extracted and plotted in figure 7. The chordwise locations of the exposed electrodes are also illustrated in the plot for clarification. As clearly shown in figure 7, the temperature profiles at the different time instants show similar distribution patterns under the different incoming airflow velocity conditions (i.e.  $U_\infty = 20 \text{ m s}^{-1}$  versus  $U_\infty = 40 \text{ m s}^{-1}$ ). While the temperature peaks were found to be located at the edges of the exposed electrodes, the maximum temperature peak is found to be generated around the fourth electrode (i.e.  $\sim 15\%$  chord length) under both testing conditions. With the AOA of the airfoil/wing model being set at  $\text{AOA} = 0^\circ$ , an obvious gradient of the surface temperature distribution is observed, i.e. a trend of temperature increasing from the leading-edge to



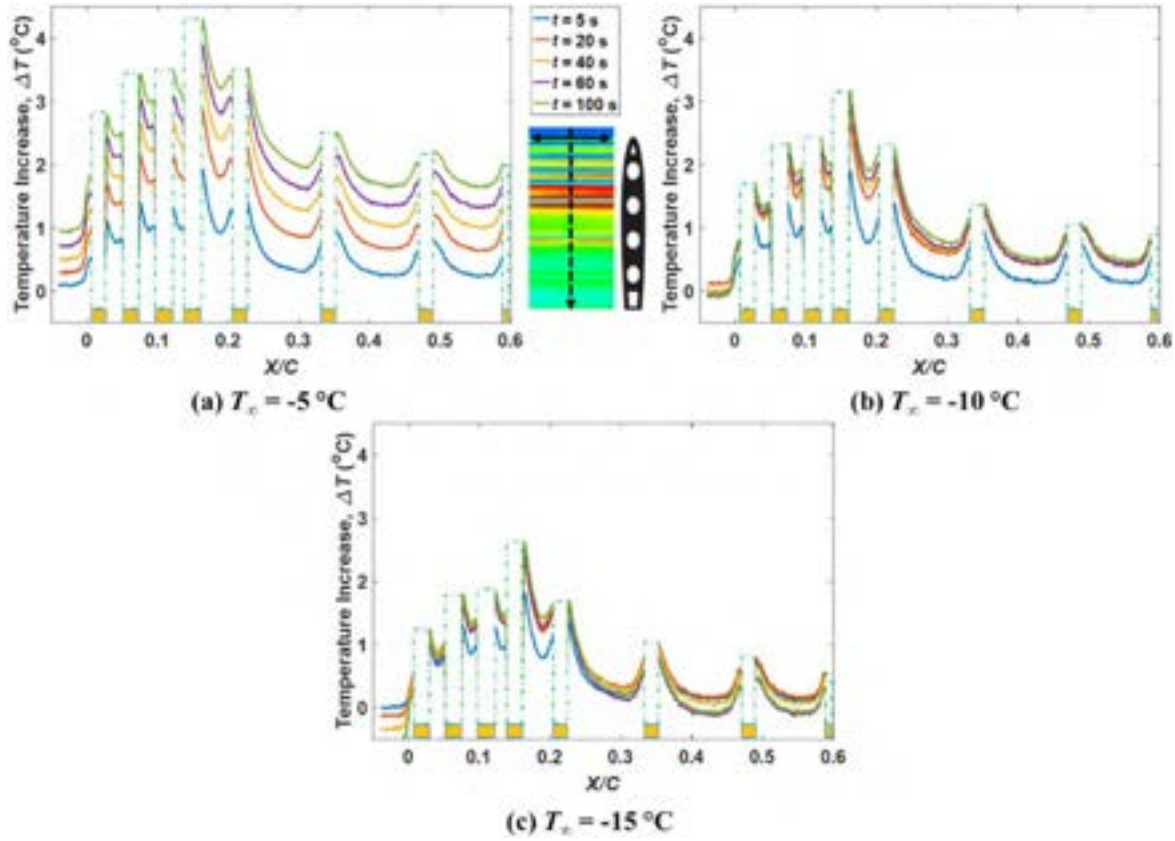


**Figure 9.** Time-evolutions of the measured surface temperature distributions over the airfoil/wing model under the test conditions of  $U_{\infty} = 40 \text{ m s}^{-1}$  and  $\text{AOA} = 0^{\circ}$ , and different air temperatures.

downstream with the temperature reaching the maximum at about 15% chord length, after which the temperature was found to decrease gradually, as shown in figures 7(a) and (b). Such temperature gradient along the chordwise direction is essentially determined by the chordwise distribution of convective heat transfer coefficients along the airfoil/wing model [7]. While the convective heat transfer coefficient is the maximum at the stagnation line (i.e. at the airfoil leading-edge when the  $\text{AOA}$  is  $0^{\circ}$ ), it decreases quickly to the minimum at about 15% chord length, after which a slight increase would occur due to the transition of the boundary layer airflow from laminar to turbulence [39]. It should be noted that while the peak temperatures at the fourth and the fifth electrodes are very close for the test condition of  $U_{\infty} = 20 \text{ m s}^{-1}$ , as shown in figure 7(a), the peak temperature at the fourth electrode comes to be the only maximum when the airflow velocity is

higher, i.e.  $U_{\infty} = 40 \text{ m s}^{-1}$ , as shown in figure 7(b). It is suggested that the increase of airflow velocity would essentially bring the location of the boundary layer transition moving further upstream [45], which results in the shift of the maximum temperature peak.

In order to further evaluate the effects of incoming airflow velocity on the heating dynamics of NS-DBD plasma actuation over the airfoil/wing surface, the time evolution profiles of the surface temperatures measured at different chordwise locations (i.e. location A at 4% chord, B at 12% chord, C at 20% chord, and D at 30% chord, as indicated in figure 8) over the airfoil/wing surface were extracted and plotted in figure 8. It is seen clearly that, when the airflow velocity is relatively low, i.e.  $U_{\infty} = 20 \text{ m s}^{-1}$ , the temperatures over the air/wing surface would keep increasing within the entire test period of 100 s as shown in



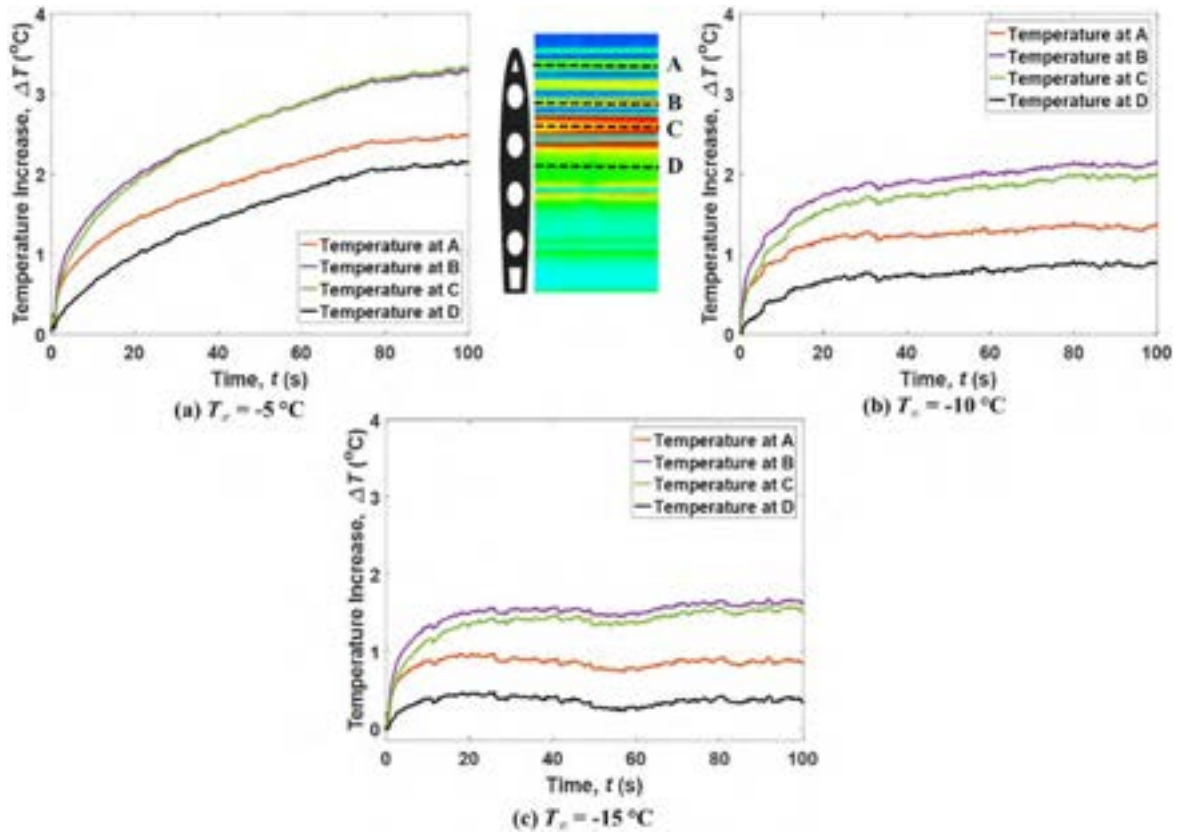
**Figure 10.** The spanwise-averaged temperature profiles along the airfoil/wing chord under the test conditions of  $U_\infty = 40 \text{ m s}^{-1}$  and  $\text{AOA} = 0^\circ$ , and different air temperatures.

figure 8(a). When the airflow velocity is increased to  $U_\infty = 40 \text{ m s}^{-1}$ , the temperatures at all the locations are found to have a smaller increase and quickly reach to the maximum (i.e. reaching the thermal equilibrium state) as shown in figure 8(b). It is suggested that the convective heat transfer would be significantly enhanced at the higher airflow velocity, which can take away more thermal energy generated in the NS-DBD plasma actuation. Thus, the temperature increase caused by the NS-DBD plasma actuation would be smaller when the airflow velocity is higher. Along with the temperature increase over the airfoil/wing surface, the temperature difference between the surface and airflow would also be increased, which results in an increase of the rate of convective heat transfer. Once the rate of heat convection to take away the thermal energy becomes equal to the rate of thermal energy generation by the NS-DBD plasma actuation, a thermal equilibrium state would be achieved with the surface temperature distribution becoming stable. For the test cases compared here, since the operating frequency of the NS-DBD plasma actuators is kept at the same as  $f = 1 \text{ kHz}$ , the rate of thermal energy generation is considered to be not changed under the different airflow velocity conditions. The smaller temperature increase and the earlier stabilization of the surface temperature distribution at the higher airflow velocity, i.e.  $U_\infty = 40 \text{ m s}^{-1}$ , are essentially caused by the faster convective heat transfer for the test case.

## 5.2. Effects of air temperature on the heating dynamics of NS-DBD plasma actuation

Figure 9 shows the time-evolutions of the measured surface temperature distributions over the airfoil/wing model with the incoming airflow velocity and the AOA of the airfoil/wing model being kept at the same of  $U_\infty = 40 \text{ m s}^{-1}$  and  $\text{AOA} = 0^\circ$  during the experiment, while the airflow temperature was changed at  $T_\infty = -5^\circ\text{C}$ ,  $-10^\circ\text{C}$  and  $-15^\circ\text{C}$ , respectively, in order to examine the effects of air temperature on the heating dynamics of NS-DBD plasma actuation over the airfoil/wing surface. It is clearly seen that, the temperature increase over the airfoil/wing surface is more evident at the higher incoming airflow temperature, i.e. while the maximum temperature increase was found to be  $\Delta T = 4^\circ\text{C}$  for the test case of  $T_\infty = -5^\circ\text{C}$ , the corresponding values become only about  $\Delta T = 3^\circ\text{C}$  and  $\Delta T = 2.5^\circ\text{C}$  for the test cases of at  $T_\infty = -10^\circ\text{C}$  and  $-15^\circ\text{C}$ , respectively. It is also found that, when the incoming airflow temperature is colder, the thermal equilibrium state over the airfoil/wing surface would be achieved earlier. More specifically, while the temperature distribution was found to become stable after about  $t = 80 \text{ s}$  for the test case with  $T_\infty = -5^\circ\text{C}$ , the duration of the surface heating (before reaching the thermal equilibrium state) was found to be about  $t = 40 \text{ s}$  and  $t = 20 \text{ s}$ , for the test cases of at  $T_\infty = -10^\circ\text{C}$  and  $-15^\circ\text{C}$ , respectively.





**Figure 11.** Time-histories of the surface temperature variations at different chordwise locations on the airfoil/wing model under the test conditions of  $U_{\infty} = 40 \text{ m s}^{-1}$  and  $\text{AOA} = 0^{\circ}$ , and different air temperatures.

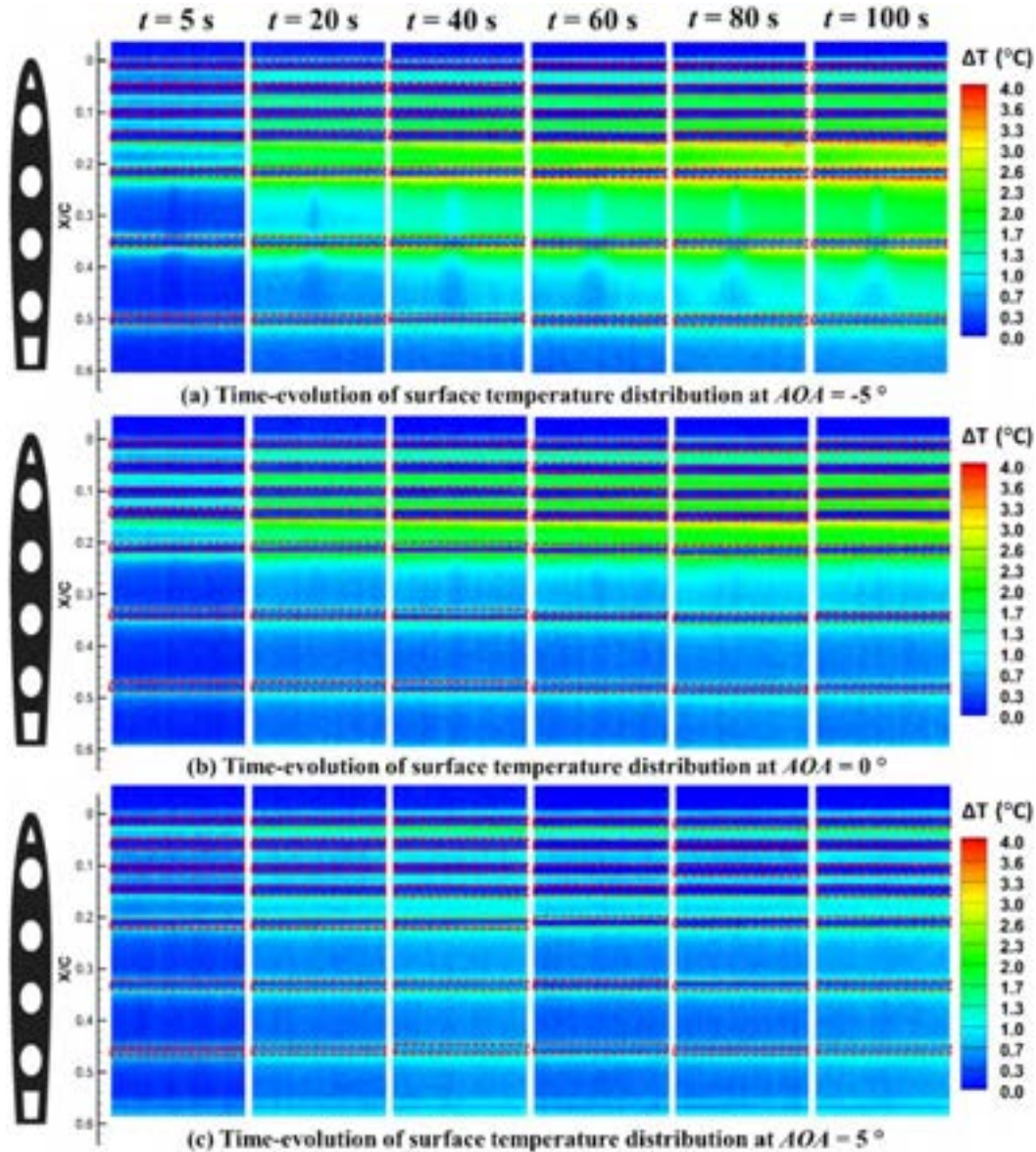
Figure 10 shows the corresponding spanwise-averaged temperature profiles along the airfoil chord at the different time instants (i.e.  $t = 5, 20, 40, 60$ , and  $100 \text{ s}$ ) extracted from the temperature distributions given in figure 9. It is seen clearly that, the temperature profiles at different time instants would follow the same pattern under the different test conditions (i.e.  $T_{\infty} = -5^{\circ}\text{C}$  to  $-10^{\circ}\text{C}$  and  $-15^{\circ}\text{C}$ ), i.e. a trend of temperature increase from the leading-edge to downstream, with the temperature reaching the maximum at about 15% chord length, after which the temperature is found to decrease gradually, as shown in figures 10(a)–(c). As mentioned above, the chordwise temperature profile along the airfoil/wing model is essentially determined by the convective heat transfer process along the chordwise direction. With the AOA of the airfoil/wing model being fixed at  $\text{AOA} = 0^{\circ}$  and the incoming airflow velocity being constant at  $U_{\infty} = 40 \text{ m s}^{-1}$ , the chordwise distributions of the convective heat transfer coefficients under the different airflow temperature conditions are suggested to be following the same profile, but with different magnitudes, i.e. larger convective heat transfer coefficient is expected at higher airflow temperatures.

Figure 11 shows the time-evolution profiles of the surface temperature measured at the different chordwise locations over the airfoil/wing surface under the different airflow temperature conditions. It is seen clearly that, when the air temperature is higher, i.e.  $T_{\infty} = -5^{\circ}\text{C}$ , the temperatures over the air/wing surface are kept increasing within the test period

of  $100 \text{ s}$  as shown in figure 11(a). As the air temperature is decreased to  $T_{\infty} = -10^{\circ}\text{C}$ , the surface temperatures at all the locations are found to have a smaller increase margin and reach to the maximum (which indicates the thermal equilibrium state) at about  $t = 40 \text{ s}$ , as shown in figure 11(b). When the airflow temperature is further decreased to  $T_{\infty} = -15^{\circ}\text{C}$ , the magnitude of the temperature increase is found to become even smaller, and reach to the peak value much earlier, i.e. at  $t = 20 \text{ s}$ . While a lower air temperature would indicate a smaller convective heat transfer coefficient due to the decelerated molecule/atom motions [39], the lower incoming airflow temperature would also cause a much faster rate of convective heat transfer due to the increased temperature difference between the airflow and the heated airfoil surface, which leads to the smaller temperature increase margin and shorter heating duration before reaching the thermal equilibrium state.

### 5.3. Effects of the AOA on the heating dynamics of NS-DBD plasma actuation

Figure 12 shows the time-evolutions of the measured surface temperature distributions over the airfoil/wing model with the velocity and temperature of the incoming airflow being constant at  $U_{\infty} = 40 \text{ m s}^{-1}$  and  $T_{\infty} = -10^{\circ}\text{C}$ , while the AOA of the airfoil/wing model was changed from  $\text{AOA} = -5^{\circ}$  to  $0^{\circ}$  and  $5^{\circ}$ , respectively. As can be seen



**Figure 12.** Time-evolutions of the measured surface temperature distributions over the airfoil/wing model under the test conditions of  $U_\infty = 40\text{ m s}^{-1}$ ,  $T_\infty = -10^\circ\text{C}$ , and (a)  $AOA = -5^\circ$ , (b)  $AOA = 0^\circ$ , and (c)  $AOA = 5^\circ$ .

clearly in figure 12, the change of AOA would significantly affect the surface temperature distribution over the airfoil/wing model, i.e. not only the magnitude of surface temperature increase, but also the distribution pattern of the chordwise temperature profiles. When the AOA of the airfoil/wing model is set to be negative, i.e.  $AOA = -5^\circ$ , the temperature increase caused by the plasma discharge is found to be relatively large, with the peak surface temperatures located in the range of  $0.15 < X/C < 0.35$ , as clearly shown in figure 12(a). When the AOA is set to be zero, while the overall temperature increase becomes smaller, in comparison to that at  $AOA = -5^\circ$ , the location of the peak surface temperature is found to move to a further upstream location, i.e.  $X/C < 0.2$ , as shown in

figure 12(b). As the AOA further increases to  $AOA = 5^\circ$ , while the surface temperature values over upper surface of the airfoil/wing model become much lower, the location of the peak temperature is found to be very near the airfoil leading-edge, as shown in figure 12(c). It is suggested that the change of AOA would essentially change the surface pressure distribution as well as the boundary layer airflow, which can dramatically affect the convective heat transfer process over the airfoil/wing upper surface, resulting in the changes of heating characteristics of the NS-DBD plasma actuation.

Figure 13 shows the corresponding spanwise-averaged temperature profiles along the airfoil chord with the airfoil/wing model mounted at different AOAs. It is seen clearly that,

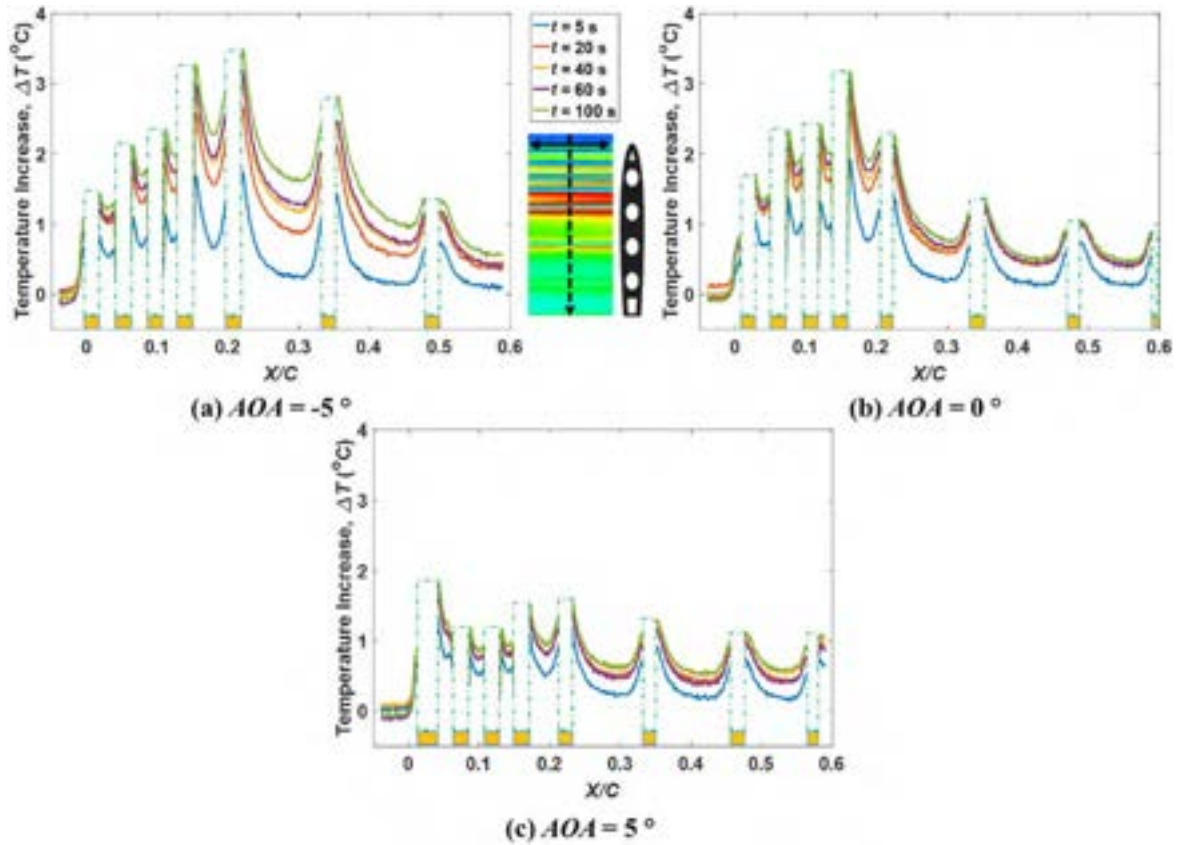


**Figure 13.** The spanwise-averaged temperature profiles along the airfoil/wing chord under the test conditions of  $U_\infty = 40 \text{ m s}^{-1}$ ,  $T_\infty = -10^\circ\text{C}$ , and (a)  $AOA = -5^\circ$ , (b)  $AOA = 0^\circ$ , and (c)  $AOA = 5^\circ$ .

as the AOA of the airfoil/wing model varies, the profile of the chordwise temperature distribution would change accordingly. When the AOA is set at  $AOA = -5^\circ$ , there is an evident temperature gradient over the upper surface of the airfoil/wing model, with the temperature increasing from the leading-edge to 20% chord length, and then decreasing gradually in the downstream locations, as shown in figure 13(a). When the airfoil/wing model is adjusted to zero AOA, though a similar pattern is observed in the chordwise temperature distribution profile, the peak surface temperature is found to be at a more upstream location, i.e.  $\sim 15\%$  chord length, as shown in figure 13(b). The temperature increase near the airfoil leading-edge is also found to become greater, in comparison to that of the test case with the negative AOA. It is suggested that, when the AOA of the airfoil/wing model is set to be negative, the stagnation line would be no longer at the airfoil leading-edge but pushed back over the upper surface of the airfoil/wing model. It can cause significant changes of the convective heat transfer over the airfoil/wing surface. As a result, the surface temperature distribution pattern over the upper surface of the airfoil/wing model would also be changed in accordance to the variations of the convective heat transfer characteristics. When the AOA of the airfoil/wing model is further increased to  $AOA = 5^\circ$ , the surface temperature distribution is found to be very different from those of the test cases with the negative and zero AOAs.

While the magnitude of the overall surface temperature increase was found to be much smaller, the peak temperature was found to be located at the leading-edge as clearly shown in figure 13(c). Such change of the surface temperature distribution pattern is suggested to be closely related to the behavior of the boundary layer airflow that is coupled with the plasma actuation over the airfoil surface.

Figure 14 shows the time-histories of the surface temperature variations at the different chordwise locations over the airfoil/wing surface at the different AOAs. It is seen clearly that, when the AOA of the airfoil/wing model is negative, i.e.  $AOA = -5^\circ$ , while the temperatures at location A and B (4% and 12% chord length) are found to be increased to the maximum (reaching the thermal equilibrium state) after about  $t = 30 \text{ s}$ , the temperatures at the downstream locations, i.e. C (20% chord length) and D (30% chord length) are found to increase almost monotonically with larger magnitudes as shown in figure 14(a). When the airfoil/wing model is set at zero AOA, while the surface temperatures at all the locations are found to increase concurrently as shown in figure 14(b), the thermal equilibrium state is found to be achieved at all locations at about  $t = 40 \text{ s}$ , with the maximum temperature increase being at location B, i.e. 12% chord length. When the AOA is changed to  $AOA = 5^\circ$ , while the magnitude of temperature increase is found to be much smaller, the thermal equilibrium state is achieved much earlier, i.e. at  $t = 20 \text{ s}$ , as



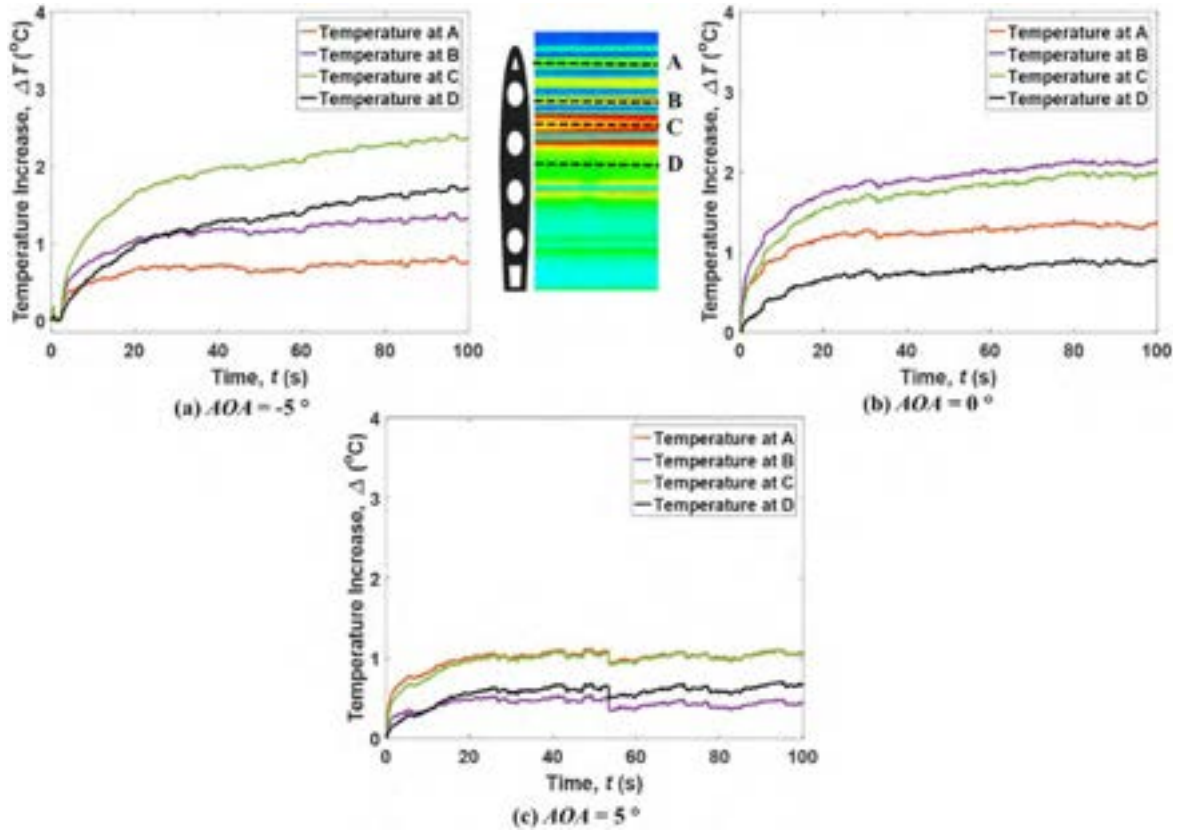


**Figure 14.** Time-histories of the surface temperature variations at different chordwise locations on the airfoil/wing model under the test conditions of  $U_\infty = 40 \text{ m s}^{-1}$ ,  $T_\infty = -10^\circ\text{C}$ , and (a)  $\text{AOA} = -5^\circ$ , (b)  $\text{AOA} = 0^\circ$ , and (c)  $\text{AOA} = 5^\circ$ .

clearly shown in figure 14(c). It is suggested the convective heat transfer over the upper surface of the airfoil/wing model would be enhanced as the AOA increases, which results in the lower temperature distribution over the surface if the same thermal energy is generated by the NS-DBD plasma actuators.

#### 5.4. Estimation of the surface heating efficiency under different test conditions

Based on the measured surface temperature variations under the different test conditions, the third stage efficiency of gas/surface heating in NS-DBD plasma discharge, i.e.  $\eta_{\text{Heat}}$ , which is defined as the ratio of effective surface heating in desired locations to the total thermal power, can be calculated using equation (40):

$$\eta_{\text{Heat}} = \frac{\rho_{\text{surf}} H_{\text{surf}} c_{\text{surf}} \Delta T}{(P_A \eta_{\text{TH}} t_{\text{heating}})/A_{\text{surf}}} = \frac{\rho_{\text{surf}} H_{\text{surf}} c_{\text{surf}}}{P_A \eta_{\text{TH}}/A_{\text{surf}}} \cdot \frac{\Delta T}{t_{\text{heating}}}, \quad (40)$$

where  $A_{\text{surf}}$  is the area of the heating surface over the airfoil/wing model.

Table 3 lists the material properties of the PVC dielectric layer as well as the input power parameters used in the present study. To accurately calculate the surface heating efficiency, the thermal efficiency,  $\eta_{\text{TH}}$ , of NS-DBD plasma discharge should be first determined. The previous literatures [31, 37, 40] have characterized the thermal efficiency of plasma discharge in various test conditions, however, a

relatively large variation (i.e.  $\eta_{\text{TH}} = 40\% - 90\%$ ) of the efficiency was obtained due to the uncertainties in measuring the thermal energy generation in the hot gas layer. Based on the parameter values given in table 3, an estimate of the surface heating efficiency,  $\eta_{\text{Heat}}$ , is calculated by using equation (40). It turns out that, the value of  $\eta_{\text{Heat}}$  is relatively small, and varies from 0.8% to 7.6%, depending on the streamwise location and the thermal efficiency set in the calculation.

In the present study, an effort was also made to calculate the normalized surface heating efficiency,  $\bar{\eta}_{\text{Heat}}$ , which is defined as the ratio of the surface heating efficiency at a streamwise location to that at the leading-edge of the airfoil/wing model. It has been revealed in Starikovskiy and Pancheshnyi [46] that the discharge power and the thermal efficiency in the plasma layer is very uniform along airfoil surfaces in NS-DBD. Therefore, the normalized surface heating efficiency can be further simplified and estimated based on the ratio of surface temperature increase at the different streamwise locations as given in equation (41):

$$\bar{\eta}_{\text{Heat}} = \frac{\left[ \frac{\rho_{\text{surf}} H_{\text{surf}} c_{\text{surf}} \Delta T}{(P_A \eta_{\text{TH}} t_{\text{heating}})/A_{\text{surf}}} \right]}{\left[ \frac{\rho_{\text{surf}} H_{\text{surf}} c_{\text{surf}} \Delta T_{\text{LE}}}{(P_A \eta_{\text{TH}} t_{\text{heating}})/A_{\text{surf}}} \right]} = \frac{\Delta T}{\Delta T_{\text{LE}}}, \quad (41)$$

where  $\Delta T_{\text{LE}}$  is the surface temperature increase at the leading-edge of the airfoil/wing model during the heating process in NS-DBD plasma actuation.

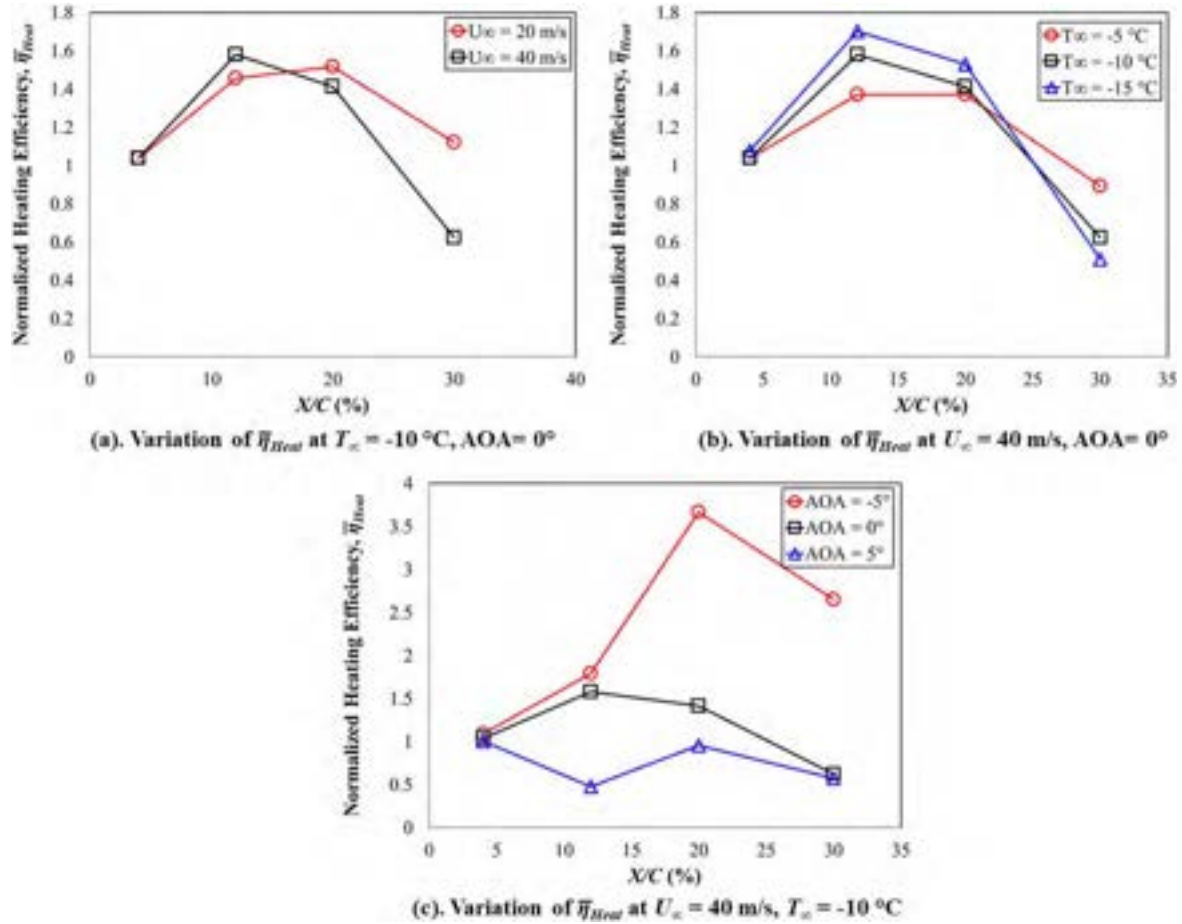


Figure 15. Streamwise variation of the normalized surface heating efficiency,  $\bar{\eta}_{Heat}$ , under different test conditions.

Figure 15 shows the streamwise variations of the normalized surface heating efficiency,  $\bar{\eta}_{Heat}$ , calculated based on the measured surface temperature distributions under the different test conditions described in the previous sections. As can be seen clearly in figure 15(a), when the airflow temperature and the AOA of the airfoil/wing model are kept the same, the increase of the airflow velocity (i.e. from  $U_{\infty} = 20$  to  $40\text{ m s}^{-1}$ ) would slightly affect the streamwise distribution of the surface heating efficiency, with the surface heating being more efficient close to the leading-edge and less efficient in downstream regions. When the airflow velocity and the AOA are kept not changed, the variation of the air temperature would also cause a change of the surface heating efficiency as clearly shown in figure 15(b). The lower air temperature tends to produce a more efficient surface heating close to the leading-edge. While both the airflow velocity and temperature are kept constant, the variation of the AOA of the airfoil/wing model would cause a significant change of the surface heating efficiency as shown in figure 15(c). When the AOA of the airfoil/wing model is set to be negative, i.e.  $AOA = -5^{\circ}$ , an evident peak of the surface heating efficiency is observed at about  $X/C = 20\%$ . When the AOA is set to be zero, the variation of the surface heating efficiency along the chordwise is much smaller. As the AOA is increased to be positive, i.e.  $AOA = 5^{\circ}$ , the surface heating is

found to become more efficient around the leading-edge region, and very inefficient in the downstream regions. It should be noted that, though the absolute values of the surface heating efficiency in NS-DBD plasma discharge are found to be very small in comparison to the conventional electro-thermal heating methods (i.e. usually have a efficiency of more than 90% [29]), it does not imply that the NS-DBD plasma actuation is not as good as the electro-thermal heating since most of the thermal energy generated in plasma discharge is stored in the gas layer near the surface, which can prevent ice formation over the airfoil/wing surface [29]. The profiles of the normalized values given in figure 15 are suggested to be great indicators of the gas heating efficiency close to the airfoil/wing surface.

## 6. Application of NS-DBD plasma actuation for aircraft icing mitigation

In the present study, the ice accretion experiments were also performed on the airfoil/wing model to evaluate the anti-/de-icing performances of the NS-DBD plasma actuators in different environmental and operational conditions. While the incoming airflow velocity and the LWC were kept not



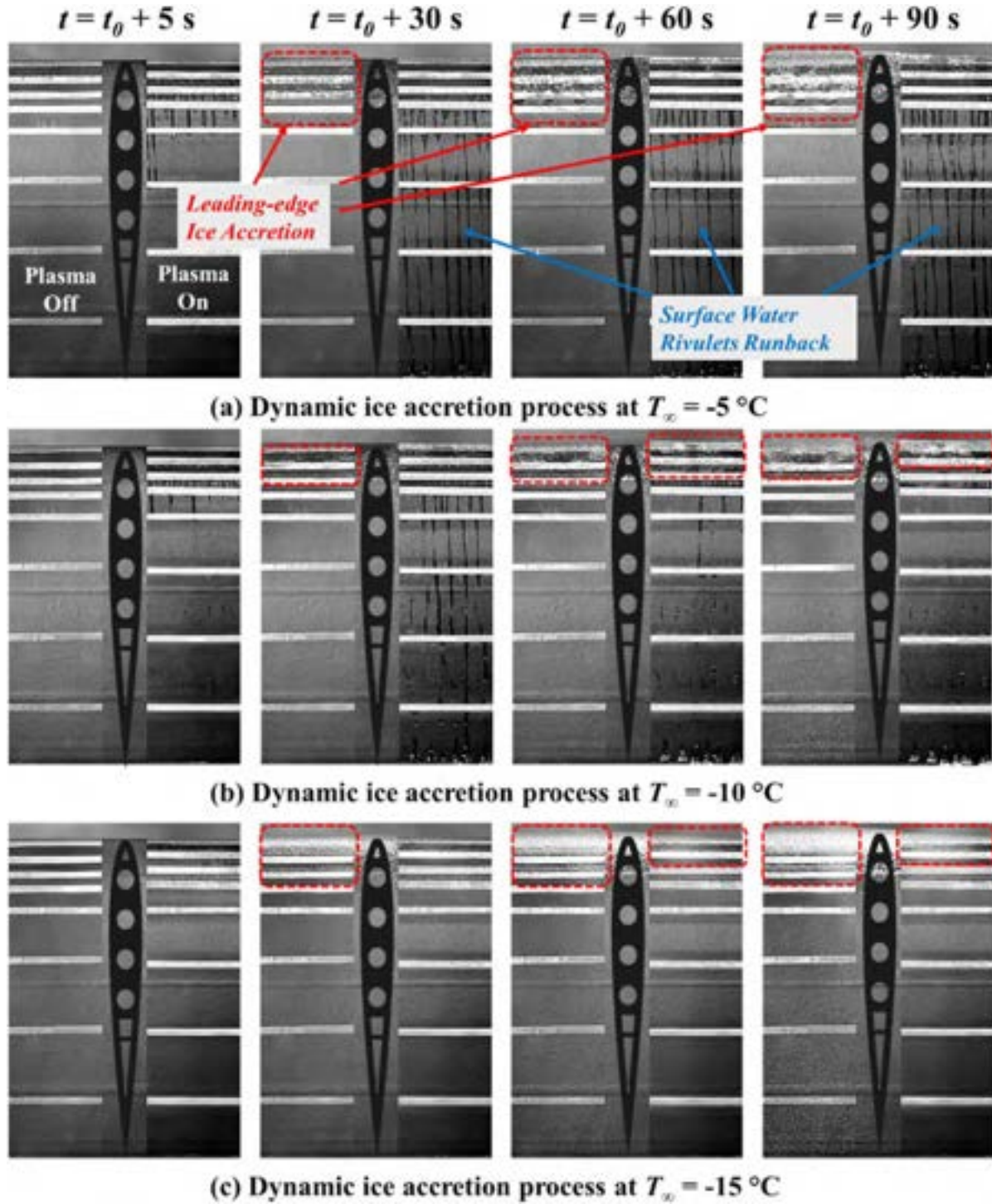


**Figure 16.** Time-evolutions of the dynamic ice accretion processes over the airfoil/wing surface under the icing conditions of  $U_{\infty} = 40 \text{ m s}^{-1}$ ,  $\text{LWC} = 1.0 \text{ g m}^{-3}$ , and (a)  $T_{\infty} = -5^{\circ}\text{C}$ , (b)  $T_{\infty} = -10^{\circ}\text{C}$ , (c)  $T_{\infty} = -15^{\circ}\text{C}$ .

changed throughout the icing experiments, i.e.  $U_{\infty} = 40 \text{ m s}^{-1}$  and  $\text{LWC} = 1.0 \text{ g m}^{-3}$ , three typical ice accretion processes (i.e. rime, mixed, and glaze icing [42]) were tested on the actuator-embedded-airfoil/wing model by changing the airflow temperature from  $-15^{\circ}\text{C}$  to  $-5^{\circ}\text{C}$ , with the operating frequency of the NS-DBD plasma actuators being varied from  $f = 2$  to  $6 \text{ kHz}$ .

#### 6.1. Anti-/de-icing performances of the NS-DBD plasma actuators in different icing conditions

Figure 16 shows the time-evolutions of the dynamic ice accretion processes over the airfoil/wing surface with the NS-DBD plasma actuation being turned on the right side of the airfoil/wing model under the different icing conditions. With the operating frequency of the NS-DBD plasma actuators

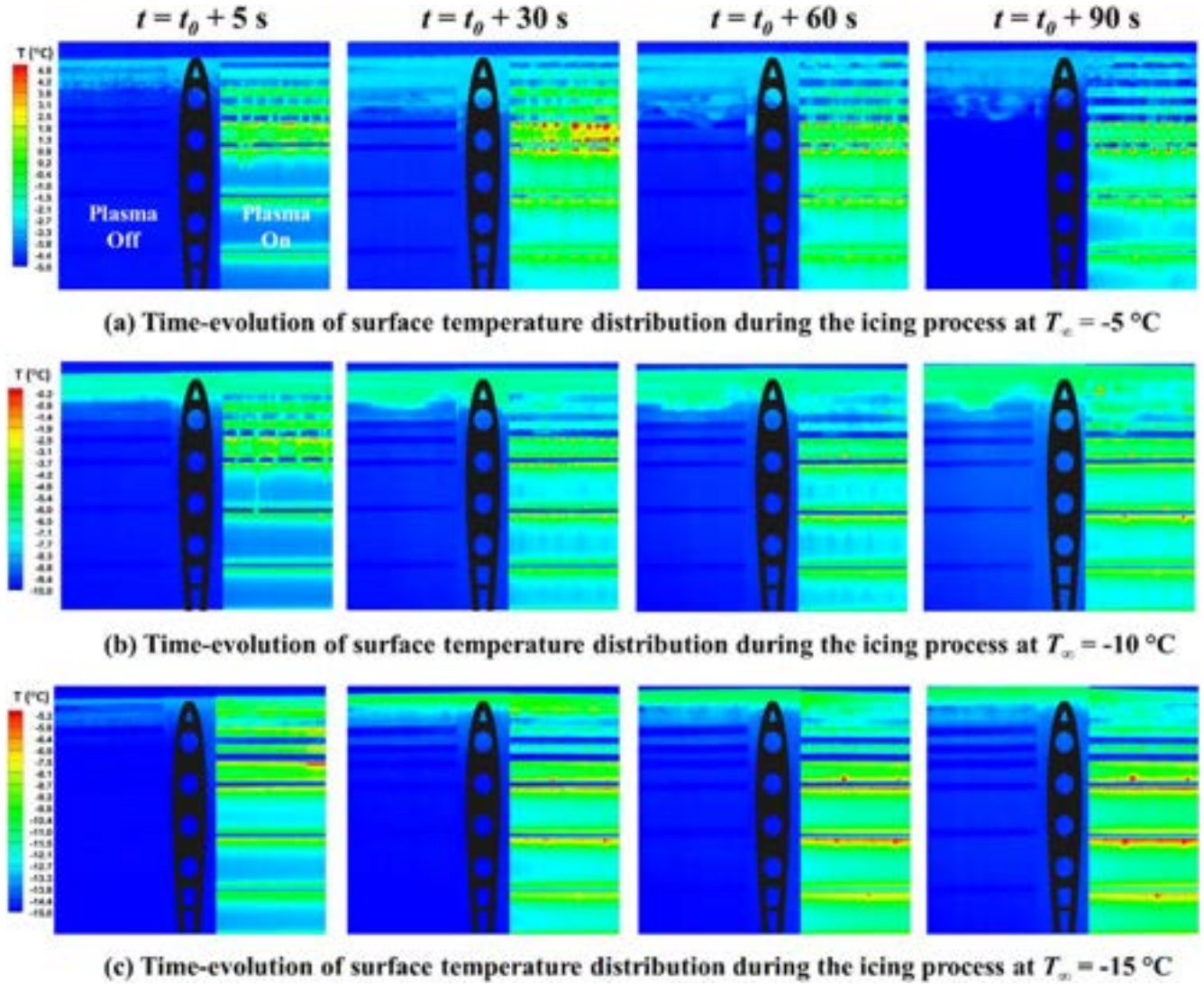


**Figure 17.** Time-evolutions of the temperature distributions over the airfoil/wing surface under the icing conditions of  $U_{\infty} = 40 \text{ m s}^{-1}$ ,  $\text{LWC} = 1.0 \text{ g m}^{-3}$ , and (a)  $T_{\infty} = -5^{\circ}\text{C}$ , (b)  $T_{\infty} = -10^{\circ}\text{C}$ , (c)  $T_{\infty} = -15^{\circ}\text{C}$ .

being fixed at  $f = 4 \text{ kHz}$ , the rate of thermal energy generation is suggested to be the same during the different ice accretion processes. The previous results have revealed that a warmer airflow temperature would produce a larger temperature increase over the airfoil/wing surface during the plasma actuation, which is suggested to promise a better anti-icing performance of the NS-DBD plasma actuators. Figure 16(a) shows the typical snapshots of the ice accreting airfoil/wing surface under the test condition of  $U_{\infty} = 40 \text{ m s}^{-1}$ ,  $\text{LWC} = 1.0 \text{ g m}^{-3}$ , and  $T_{\infty} = -5^{\circ}\text{C}$ . The corresponding surface temperature distribution is given in figure 17(a). It is clearly seen that, at the early stage of the ice accretion process, i.e.  $t = 5 \text{ s}$ , when the supercooled water droplets impinge onto the airfoil/wing surface, while the impinging water on the right side of the airfoil (with the plasma actuators turned on) is instantly heated by absorbing the thermal energy generated in the NS-DBD plasma actuation, the impinging water droplets on the left side of the airfoil model (with the plasma actuators turned off) are found to be frozen partially with the remaining water mass being transported and frozen

in near downstream. As a result, while evident surface water rivulets are found to be formed on the right side, a typical glaze ice accretion is observed on the left side of the airfoil/wing model. As the time goes by, with more and more water droplets impinge on the airfoil/wing surface, the glaze ice accreted around the leading-edge is found to become thicker and thicker as indicated in the red dashed boxes shown in figure 16(a). In the mean time, the impinging water on the right side is continuously heated, forming the steady rivulet channels as indicated in figure 16(a). Based on the corresponding temperature distributions of the ice accreting airfoil/wing surface shown in figure 17(a), it can be found that while the NS-DBD plasma actuation is found to generate thermal energy to keep the impinging water warm and in the liquid state, the maximum temperature is located around 20% chord length, which is beyond the direct impingement region of the water droplets. The thermal energy generated during the plasma actuation in this case is therefore considered to be not fully occupied for melting the impinging water/ice accumulation around the leading-edge. Thus, the NS-DBD



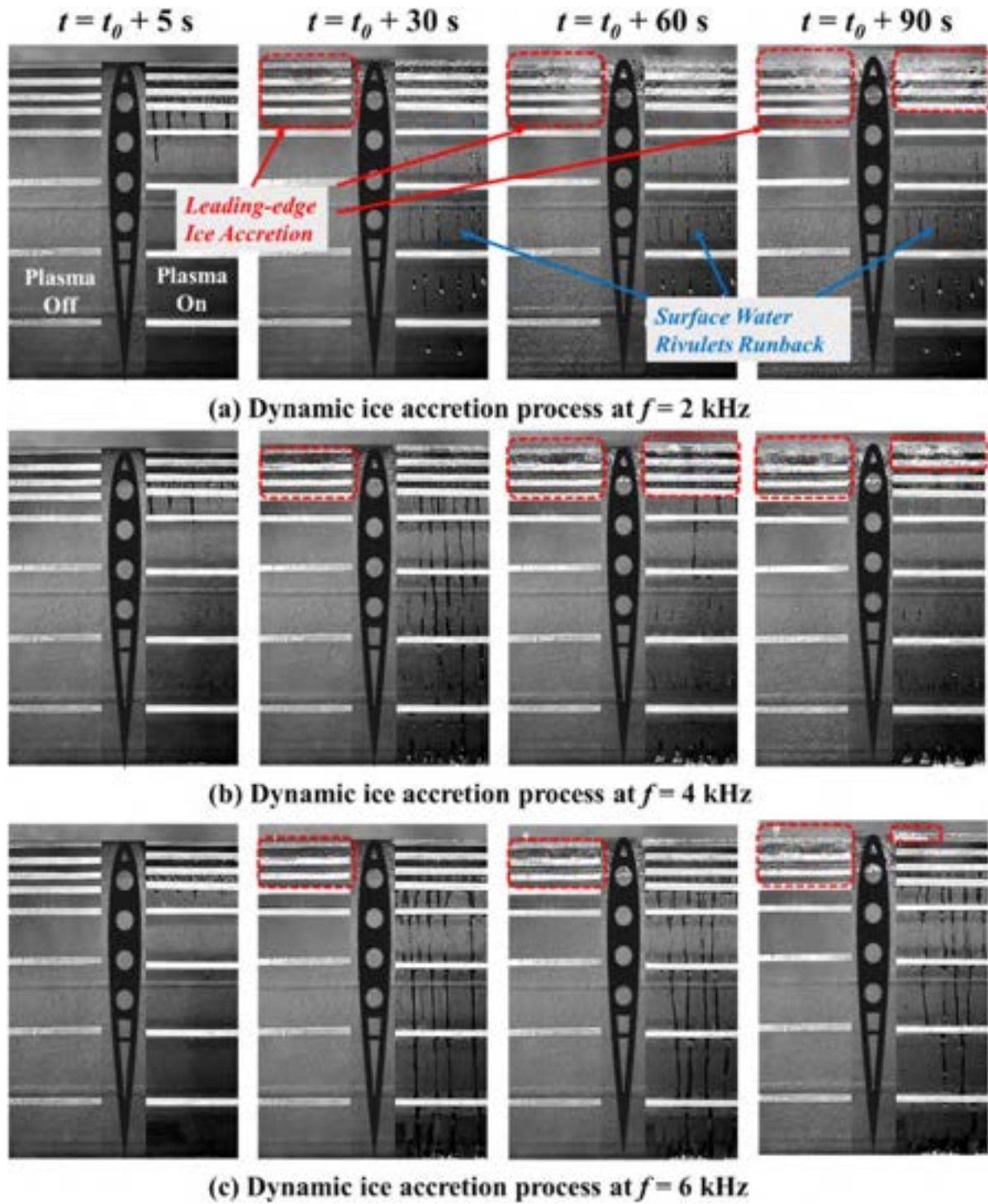


**Figure 18.** Time-evolutions of the dynamic ice accretion processes over the airfoil/wing surface under the icing conditions of  $U_\infty = 40 \text{ m s}^{-1}$ ,  $\text{LWC} = 1.0 \text{ g m}^{-3}$ , and  $T_\infty = -10^\circ\text{C}$ , with the NS-DBD plasma actuators being operated at (a)  $f = 2$  kHz, (b)  $f = 4$  kHz, and (c)  $f = 6$  kHz.

plasma actuators over the airfoil/wing surface are suggested to be further modified to have more thermal energy generation around the leading-edge and less in the downstream locations to efficiently prevent ice formation/accretion at the leading-edge and avoid water refreezing over the downstream surfaces.

When the air temperature was decreased to  $T_\infty = -10^\circ\text{C}$ , a typical mixed ice accretion was generated over the airfoil/wing surface. It is clearly seen that though the thermal energy is still generated on the right side of the airfoil/wing model by the NS-DBD plasma actuators, an ice layer is found to be formed. This is suggested to be caused by the insufficient thermal

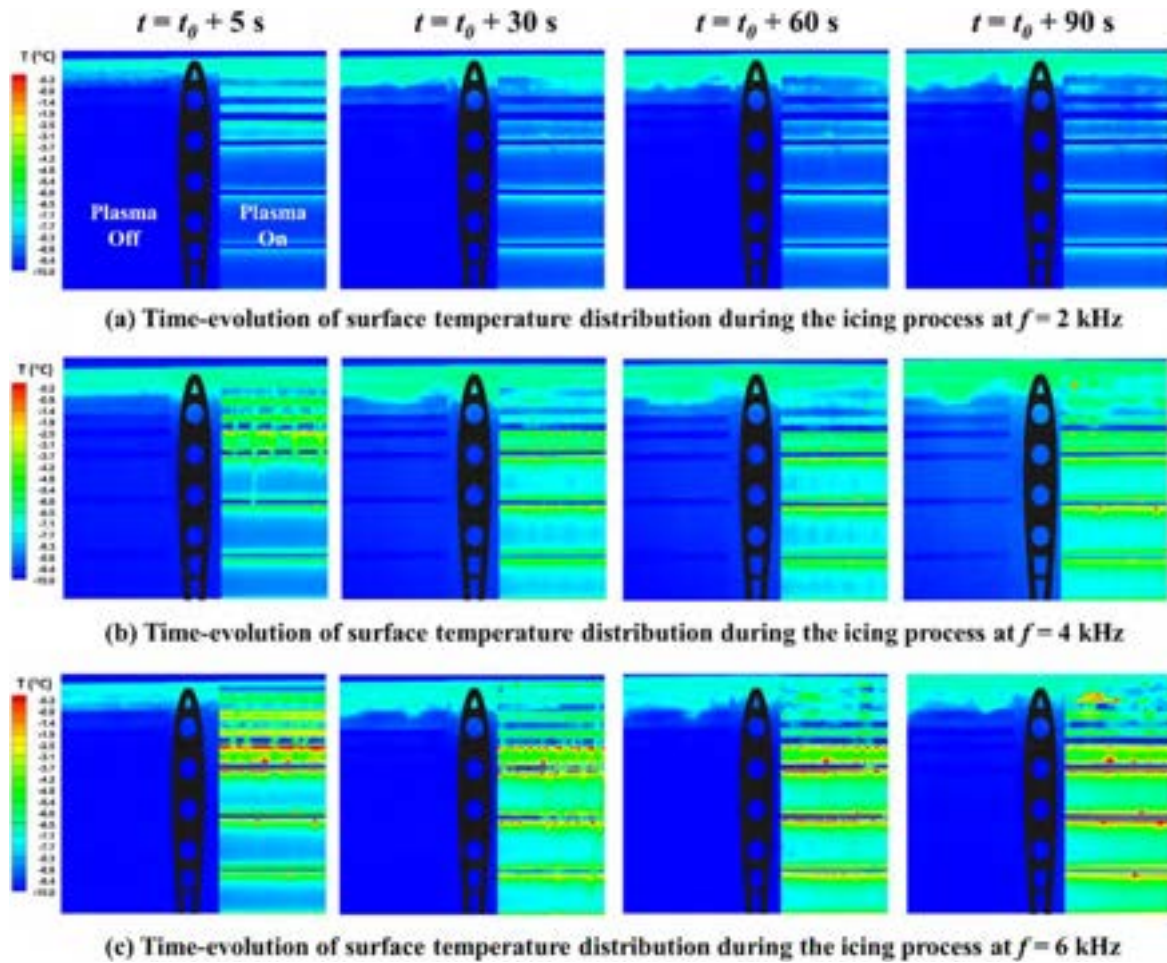


**Figure 19.** Time-evolutions of the temperature distributions over the airfoil/wing surface under the icing conditions of  $U_{\infty} = 40 \text{ m s}^{-1}$ ,  $\text{LWC} = 1.0 \text{ g m}^{-3}$ , and  $T_{\infty} = -10^{\circ}\text{C}$ , with the NS-DBD plasma actuators being operated at (a)  $f = 2$  kHz, (b)  $f = 4$  kHz, and (c)  $f = 6$  kHz.

energy to melt the ice layer and compete with the strong convective heat transfer around the leading-edge area. Once the ice layer is formed over the exposed electrodes, less plasma discharge would be formed, and therefore less thermal energy would be generated at these locations. As a result, a large amount of ice is found to be formed on both sides of the airfoil/wing model as shown in figure 16(b). Based on the corresponding temperature distributions shown in figure 17(b), it can be found that after the ice accreted on the electrode surfaces, the local temperatures around the exposed electrodes are kept very low and below zero, which is corresponding to the ice formation at these locations. In this case, though the downstream region is still heated throughout the icing process, less water mass would reach to these locations, causing a loss of efficiency in utilizing the thermal energy generated during the plasma actuation. As the air temperature is further decreased, i.e.  $T_{\infty} = -15^{\circ}\text{C}$ , a typical rime ice formation is observed as clearly shown in figure 16(c). For the NS-DBD plasma actuation in this case, due to the much faster rate of convective heat transfer, the surface temperature over the right side of the airfoil/wing surface is found to be only increased slightly as shown in figure 17(c). Thus, though the same amount of thermal energy is generated, due to the reduced surface heating

efficiency of the plasma actuation at the lower air temperature, ice is still found to be formed around the leading-edge as clearly shown in figure 16(c).

## 6.2. Anti-/De-icing performances of the NS-DBD plasma actuators at different operating frequencies

Figure 18 shows the time-evolutions of the dynamic ice accretion processes over the airfoil/wing surface under the icing condition of  $U_{\infty} = 40 \text{ m s}^{-1}$ ,  $\text{LWC} = 1.0 \text{ g m}^{-3}$ , and  $T_{\infty} = -10^{\circ}\text{C}$ , but with the NS-DBD plasma actuation being operated at different pulse frequencies (i.e.  $f = 2$  kHz, 4 kHz, and 6 kHz). The corresponding surface temperature distributions of the ice accreting airfoil/wing surface are given in figure 19. As can be seen clearly in figure 18, along with the increase of the operating frequency of the NS-DBD plasma actuators, the amount of ice accretion on the right side of the airfoil/wing model is found to become less and less. Since the power of the NS-DBD plasma actuators is linearly related to the nanosecond pulse frequency, more thermal energy would be generated over the ice accreting airfoil/wing surface at higher operating frequencies as indicated by the higher temperature distributions given in figure 19.

When the pulse frequency is relatively low, i.e.  $f = 2$  kHz, as the supercooled water droplets impinge onto the airfoil surface, since the thermal energy generated by the NS-DBD plasma actuation is not enough to compete with the strong convective heat transfer and keep the impinged water in the liquid state, an ice layer is found to be quickly formed around the leading-edge of the airfoil/wing model as shown in figure 18(a). As the time goes by, less plasma discharge would be generated over the region covered by the ice layer, which is indicated by the low temperature around the leading-edge as shown in figure 19(a). Thus, more and more impinged water is found to be frozen over the ice accreting surface, resulting in the large amount of ice accretion as shown in figure 18(a). As the pulse frequency of the NS-DBD plasma actuators is increased to  $f = 4$  kHz, double of the thermal energy would be generated over the airfoil/wing surface as indicated by the higher temperature distribution shown in figure 19(b). The increased thermal energy generation is found to significantly reduce the amount of ice accretion around the leading-edge as shown in figure 18(b). When the pulse frequency is further increased to  $f = 6$  kHz, as can be seen clearly in figure 18(c), there is almost no ice formation around the leading-edge of the airfoil/wing model, which is essentially due to the much more thermal energy generation during the plasma actuation at the higher operating frequency. However, it should be noted, along with the increase of the pulse frequency of the NS-DBD plasma actuators, the thermal energy generation would be increased all over the airfoil/wing surface. As mentioned above, the impingement of the supercooled water droplets is mainly concentrated around the leading-edge, which requires more energy to prevent ice formation. Therefore, the current configuration of the plasma actuators is suggested to be further optimized based on the convective heat transfer characteristics as well as the water impingement distribution and the associated surface water transport behaviors. Furthermore, the three-electrode NS-DBD configuration is also suggested [47, 48] to improve the anti-/de-icing efficiency by elongating the streamer propagation and the effective heating area especially close to the leading-edge.

## 7. Conclusion

In the present study, a comprehensive experimental study was conducted to examine the thermal characteristics of NS-DBD plasma actuation over an airfoil/wing surface and to evaluate the potential of NS-DBD plasma actuators for aircraft in-flight icing mitigation. The explorative study was conducted in the unique Icing Research Tunnel available at Iowa State University (i.e. ISU-IRT). While the transient thermal characteristics of NS-DBD plasma actuation over the airfoil/wing model were quantified by using an IR thermal imaging system, the anti-icing performances of the NS-DBD plasma actuators under different icing conditions, i.e. rime, mixed, and glaze, were evaluated based on the images of the dynamic ice accretion process over the

airfoil/wing surface acquired with a high-resolution/high-speed imaging system. The effects of incoming airflow velocity, airflow temperature, and AOA of the airfoil/wing model on the thermal characteristics of NS-DBD plasma actuation as well as the anti-/de-icing performances of the NS-DBD plasma actuators were systematically investigated under different icing conditions.

It is found that the dynamic heating process induced by the NS-DBD plasma actuation over the airfoil/wing surface is strongly dependent on the relevant operation parameters, including the velocity and temperature incoming airflow and the AOA of the airfoil/wing model. While the increase of the incoming airflow velocity was found to enhance the convective heat transfer, resulting in a lower temperature distribution over the airfoil/wing surface, the decrease of the air temperature was found to reduce the surface heating of the NS-DBD plasma actuation. Along with the reduction of the surface heating efficiency during the plasma actuation, the thermal equilibrium state was also found to be achieved much earlier at the higher incoming airflow velocity and lower airflow temperatures. It was also found that the characteristics of the surface temperature distribution induced by the heating of NS-DBD plasma actuation would vary significantly as the AOA of the airfoil/wing model is changed. While the surface heating efficiency of NS-DBD plasma over the upper surface of the airfoil/wing model is found to increase at the negative AOA, i.e.  $\text{AOA} = -5^\circ$ , less temperature increase was observed when the AOA of the airfoil/wing model becomes positive, i.e.  $\text{AOA} = 5^\circ$ .

The ice accretion experiments revealed clearly that, for the same input pulse frequency, the NS-DBD plasma actuation would have a better anti-/de-icing performance at the warmer air temperatures, i.e.  $T_\infty = -5^\circ\text{C}$ , due to the higher heating efficiency of the NS-DBD plasma actuation. It is suggested that the anti-icing performance of the NS-DBD plasma actuators can be improved by increasing the pulse frequency of the NS-DBD plasma actuations. The findings derived from the present study are believed to be very helpful to explore/optimize design paradigms for the development novel plasma-based anti-/de-icing strategies tailored specifically for aircraft inflight icing mitigation to ensure safer and more efficient aircraft operation in atmospheric icing conditions.

## Acknowledgments

The research work is partially supported by Iowa Space Grant Consortium (ISGC) Base Program for Aircraft Icing Studies and National Science Foundation (NSF) under award numbers of CBET-1064196 and CBET-1435590.

## ORCID iDs

Yang Liu  <https://orcid.org/0000-0003-0289-3837>  
 Andrey Y Starikovskiy  <https://orcid.org/0000-0002-5780-5681>



## References

- [1] Cebeci T and Kafyeke F 2003 Aircraft icing *Annu. Rev. Fluid Mech.* **35** 11–21
- [2] Bragg M, Gregorek G and Lee J 1986 Airfoil aerodynamics in icing conditions *J. Aircr.* **23** 76–81
- [3] Potapczuk M G 2013 Aircraft icing research at NASA glenn research center *J. Aerosp. Eng.* **26** 260–76
- [4] Politovich M K 1989 Aircraft icing caused by large supercooled droplets *J. Appl. Meteorol.* **28** 856–68
- [5] Liu Y, Bond L J and Hu H 2017 Ultrasonic-attenuation-based technique for ice characterization pertinent to aircraft icing phenomena *AIAA J.* **55** 1–8
- [6] Hansman R J and Kirby M S 1987 Comparison of wet and dry growth in artificial and flight icing conditions *J. Thermophys. Heat Transf.* **1** 215–21
- [7] Liu Y and Hu H 2018 An experimental investigation on the unsteady heat transfer process over an ice accreting airfoil surface *Int. J. Heat Mass Transf.* **122** 707–18
- [8] Liu Y, Chen W-L, Bond L J and Hu H 2017 An experimental study on the characteristics of wind-driven surface water film flows by using a multi-transducer ultrasonic pulse-echo technique *Phys. Fluids* **29** 012102
- [9] Thomas S K, Cassoni R P and MacArthur C D 1996 Aircraft anti-icing and de-icing techniques and modeling *J. Aircr.* **33** 841–54
- [10] Ramakrishna D M and Viraraghavan T 2005 Environmental impact of chemical deicers—a review *Water Air Soil Pollut.* **166** 49–63
- [11] Liu Y, Li L, Li H and Hu H 2018 An experimental study of surface wettability effects on dynamic ice accretion process over an UAS propeller model *Aerosp. Sci. Technol.* **73** 164–72
- [12] Liu Y, Ma L, Wang W, Kota A K and Hu H 2018 An experimental study on soft PDMS materials for aircraft icing mitigation *Appl. Surf. Sci.* **447** 599–609
- [13] Antonini C, Innocenti M, Horn T, Marengo M and Amirfazli A 2011 Understanding the effect of superhydrophobic coatings on energy reduction in anti-icing systems *Cold Reg. Sci. Technol.* **67** 58–67
- [14] Cao L, Jones A K, Sikka V K, Wu J and Gao D 2009 Anti-icing superhydrophobic coatings *Langmuir* **25** 12444–8
- [15] Golovin K, Kobaku S P R, Lee D H, DiLoreto E T, Mabry J M and Tuteja A 2016 Designing durable icephobic surfaces *Sci. Adv.* **2** e1501496–1501496
- [16] Sojoudi H et al 2016 Durable and scalable icephobic surfaces: similarities and distinctions from superhydrophobic surfaces *Soft Matter* **12** 1938–63
- [17] Beemer D L, Wang W, Kota A K, Doi M, Brochard-Wyart F, Tuteja A, Aizenberg J, Wang J, Song Y and Jiang L 2016 Durable gels with ultra-low adhesion to ice *J. Mater. Chem. A* **4** 18253–8
- [18] Pourbagian M and Habashi W G 2015 Aero-thermal optimization of in-flight electro-thermal ice protection systems in transient de-icing mode *Int. J. Heat Fluid Flow* **54** 167–82
- [19] Fakorede O, Ibrahim H, Ilinca A and Perron J 2016 Experimental investigation of power requirements for wind turbines electrothermal anti-icing systems *Wind Turbines—Design, Control and Applications* (London: IntechOpen) (<https://doi.org/10.5772/63449>)
- [20] Dong W, Zhu J, Zheng M and Chen Y 2015 Thermal analysis and testing of nonrotating cone with hot-air anti-icing system *J. Propuls. Power* **31** 896–903
- [21] Zhou W, Liu Y, Hu H, Hu H and Meng X 2018 Utilization of thermal effect induced by plasma generation for aircraft icing mitigation *AIAA J.* **56** 1097–104
- [22] Cai J, Tian Y, Meng X, Han X, Zhang D and Hu H 2017 An experimental study of icing control using DBD plasma actuator *Exp. Fluids* **58** 102
- [23] Wang J-J, Choi K-S, Feng L-H, Jukes T N and Whalley R D 2013 Recent developments in DBD plasma flow control *Prog. Aerosp. Sci.* **62** 52–78
- [24] Jousot R, Lago V and Parisse J-D 2015 Quantification of the effect of surface heating on shock wave modification by a plasma actuator in a low-density supersonic flow over a flat plate *Exp. Fluids* **56** 102
- [25] Corke T C, Enloe C L and Wilkinson S P 2010 Dielectric barrier discharge plasma actuators for flow control *Annu. Rev. Fluid Mech.* **42** 505–29
- [26] Roupasov D V, Nikipelov A A, Nudnova M M and Starikovskii A Y 2009 Flow separation control by plasma actuator with nanosecond pulsed-periodic discharge *AIAA J.* **47** 168–85
- [27] Stanfield S A, Menart J, DeJoseph C, Kimmel R L and Hayes J R 2009 Rotational and vibrational temperature distributions for a dielectric barrier discharge in air *AIAA J.* **47** 1107–15
- [28] Dong B, Bauchire J M, Pouvesle J M, Magnier P and Hong D 2008 Experimental study of a DBD surface discharge for the active control of subsonic airflow *J. Phys. D: Appl. Phys.* **41** 155201
- [29] Liu Y, Kolbakir C, Hu H and Hu H 2018 A comparison study on the thermal effects in DBD plasma actuation and electrical heating for aircraft icing mitigation *Int. J. Heat Mass Transf.* **124** 319–30
- [30] Zhu Y, Wu Y, Cui W, Li Y and Jia M 2013 Numerical investigation of energy transfer for fast gas heating in an atmospheric nanosecond-pulsed DBD under different negative slopes *J. Phys. D: Appl. Phys.* **46** 495205
- [31] Van den B J 2016 *Efficiency and De-icing Capability of Nanosecond Pulsed Dielectric Barrier Discharge Plasma Actuators* (Delft University of Technology) Ph.D. Dissertation
- [32] Kolbakir C, Liu Y, Hu H, Starikovskiy A and Miles R B 2018 An experimental investigation on the thermal effects of NS-DBD and AC-DBD plasma actuators for aircraft icing mitigation *2018 AIAA Aerospace Sciences Meeting* (Reston, Virginia: American Institute of Aeronautics and Astronautics)
- [33] Starikovskii A Y, Nikipelov A A, Nudnova M M and Roupasov D V 2009 SDBD plasma actuator with nanosecond pulse-periodic discharge *Plasma Sources Sci. Technol.* **18** 034015
- [34] Leonov S B, Petrishchev V and Adamovich I V 2014 Dynamics of energy coupling and thermalization in barrier discharges over dielectric and weakly conducting surfaces on  $\mu$ s to ms time scales *J. Phys. D: Appl. Phys.* **47** 465201
- [35] Tirumala R, Benard N, Moreau E, Fenot M, Lalizel G and Dornnac E 2014 Temperature characterization of dielectric barrier discharge actuators: influence of electrical and geometric parameters *J. Phys. D: Appl. Phys.* **47** 255203
- [36] Popov N A 2001 Investigation of the mechanism for rapid heating of nitrogen and air in gas discharges *Plasma Phys. Rep.* **27** 886–96
- [37] Aleksandrov N L, Kindysheva S V, Nudnova M M and Starikovskiy A Y 2010 Mechanism of ultra-fast heating in a non-equilibrium weakly ionized air discharge plasma in high electric fields *J. Phys. D: Appl. Phys.* **43** 255201
- [38] Nudnova M M, Kindysheva S V, Aleksandrov N L and Starikovskii A Y 2015 Fast gas heating in  $N_2/O_2$  mixtures under nanosecond surface dielectric barrier discharge: the effects of gas pressure and composition *Phil. Trans. A* **373**
- [39] Incropera F P 2011 *Fundamentals of Heat and Mass Transfer* (New York: Wiley)
- [40] Correale G, Avallone F and Starikovskiy A Y 2016 Experimental method to quantify the efficiency of the first two operational stages of nanosecond dielectric barrier discharge plasma actuators *J. Phys. D: Appl. Phys.* **49** 505201

- [41] Waldman R M and Hu H 2015 High-speed imaging to quantify transient ice accretion process over an airfoil *J. Aircr.* **53** 369–77
- [42] Liu Y, Li L, Ning Z, Tian W and Hu H 2018 Experimental investigation on the dynamic icing process over a rotating propeller model *J. Propuls. Power* **1**–14
- [43] Soloff S M, Adrian R J and Liu Z-C 1997 Distortion compensation for generalized stereoscopic particle image velocimetry *Meas. Sci. Technol.* **8** 1441–54
- [44] Jousset R, Boucinha V, Weber-Rozenbaum R, Rabat H, Leroy-Chesneau A and Hong D 2010 Thermal characterization of a DBD plasma actuator: dielectric temperature measurements using infrared thermography *40th Fluid Dynamics Conf. and Exhibit* (Reston, Virginia: American Institute of Aeronautics and Astronautics)
- [45] Anderson J D Jr 2010 *Fundamentals of Aerodynamics* (New-York: McGraw-Hill)
- [46] Starikovskiy A and Pancheshnyi S 2013 Dielectric barrier discharge development at low and moderate pressure conditions *51st AIAA Aerospace Sciences Meeting Including the New Horizons Forum and Aerospace Exposition* (Reston, Virginia: American Institute of Aeronautics and Astronautics)
- [47] Bayoda K D, Benard N and Moreau E 2015 Nanosecond pulsed sliding dielectric barrier discharge plasma actuator for airflow control: electrical, optical, and mechanical characteristics *J. Appl. Phys.* **118** 063301
- [48] Kourtzanidis K and Raja L L 2017 Three-electrode sliding nanosecond dielectric barrier discharge actuator: modeling and physics *AIAA J.* **55** 1393–404